Sustainable
Energy & Fuels

ROYAL SOCIETY
OF CHEMISTRY

REVIEW

View Article Online
View Journal | View Issue

Check for updates

Cite this: *Sustainable Energy Fuels*, 2025, **9**, 2625

Received 9th January 2025
Accepted 26th March 2025

DOI: 10.1039/d5se00028a

rsc.li/sustainable-energy

Advantages of ordered catalyst layers in PEMFCs: theoretical perspectives and future development

Muhammad Yusro *[a,b] and Viktor Hacker [a]

The catalyst layer in Proton Exchange Membrane Fuel Cells (PEMFCs) is crucial for facilitating electrochemical reactions. These layers required meticulously engineered structures to optimize the accessibility of catalyst sites to reactants and to enhance electron and proton transport. The advancement of patterned ordered catalyst layers has attracted significant attention, as this arrangement is thought to resolve essential challenges relative to conventional catalyst layer structures in fuel cells. The theoretical foundation for the usage of ordered catalyst layers and their superior performance has not yet been documented. This article addresses the implications of shifting from conventional catalyst layers (CCLs) to ordered catalyst layers (OCLs) in PEMFC applications. The discussion will address important aspects, including mass transfer, reaction rates, platinum utilization, water management, and the generation of electricity, which are essential for interpreting the performance of PEMFCs. Future directions involve modeling, manufacturing scalability, inventive structural designs, and the dissemination of developments, providing insights into enhancing the performance and practicality of PEMFCs.

1. Introduction

Climate change, primarily caused by greenhouse gas (GHG) emissions, represents a significant threat to world ecosystems, economies, and human health. Global energy-related CO_2 emissions hit an all-time high of 37 gigatonnes in 2022, highlighting an urgent need for swift changes to alleviate these negative consequences.[1] Global initiatives including the Paris Agreement underscore the importance of constraining global temperature increase to 1.5 °C above pre-industrial levels, demanding achieving the target of net-zero emissions by 2050.[2] To achieve this objective, renewable energy technologies must displace carbon-intensive systems, prioritizing clean alternatives for energy generation and consumption. Hydrogen energy systems are attracting interest for their potential to remove energy production from carbon emissions, positioning them as a source of zero-emission alternatives. The International Energy Agency (IEA) estimates that hydrogen could fulfill over 22% of world energy consumption by 2050, leading to a reduction in annual CO_2 emissions by 80 gigatons.[3]

Fuel cells are one example of a hydrogen-powered technology. Proton Exchange Membrane Fuel Cells (PEMFCs), an established type of fuel cell, are highly advantageous owing to their high efficiency, small construction, and environmental friendliness. PEMFC systems operate at low temperatures (60–80 °C) and higher temperatures (120–200 °C).[4] The basic operation of PEMFCs is based on the electrochemical reactions taking place at the anode and cathode, combined with a proton exchange membrane (PEM). This structure, identified as the membrane electrode assembly (MEA), incorporates the gas diffusion layer (GDL).

The schematic diagram of a PEMFC is seen in Fig. 1. At the anode, hydrogen molecules (H_2) are dissociated into protons (H^+) and electrons (e^-) *via* a catalytic process. Protons pass the membrane, whereas electrons travel through an external circuit, producing electricity. At the cathode, oxygen molecules (O_2) perform a reaction with protons and electrons to produce water. The following highlights these reactions:

$$\text{Anode: } 2H_2 \rightarrow 4H^+ + 4e^-$$

$$\text{Cathode: } O_2 + 4H^+ + 4e^- \rightarrow 2H_2O$$

The high cost of platinum (Pt)-based catalysts stands for an important issue for PEMFCs. The U.S. Department of Energy (DOE) strives to reduce platinum content and loading to 0.125 mg cm^{-2} by 2020;[5] however, most existing proton exchange membrane fuel cells (PEMFCs) necessitate approximately 0.25–0.5 mg cm^{-2} to sustain performance in vehicle applications.[6] The cost of platinum constitutes over 40% of total fuel cell expenses,[7] presenting a considerable challenge to commercialization.

Along with cost, conventional catalyst layers encounter suboptimal mass transport and unfit catalyst utilization.[8] The random distribution of catalyst particles within these layers of catalysts frequently results in uneven reactions and increased

---

[a] *Institute of Chemical Engineering and Environmental Technology, TU Graz, 8010, Austria. E-mail: yusro@student.tugraz.at*

[b] *Telkom University, Jalan D.I. Panjaitan 128, Purwokerto 53147, Central Java, Indonesia*

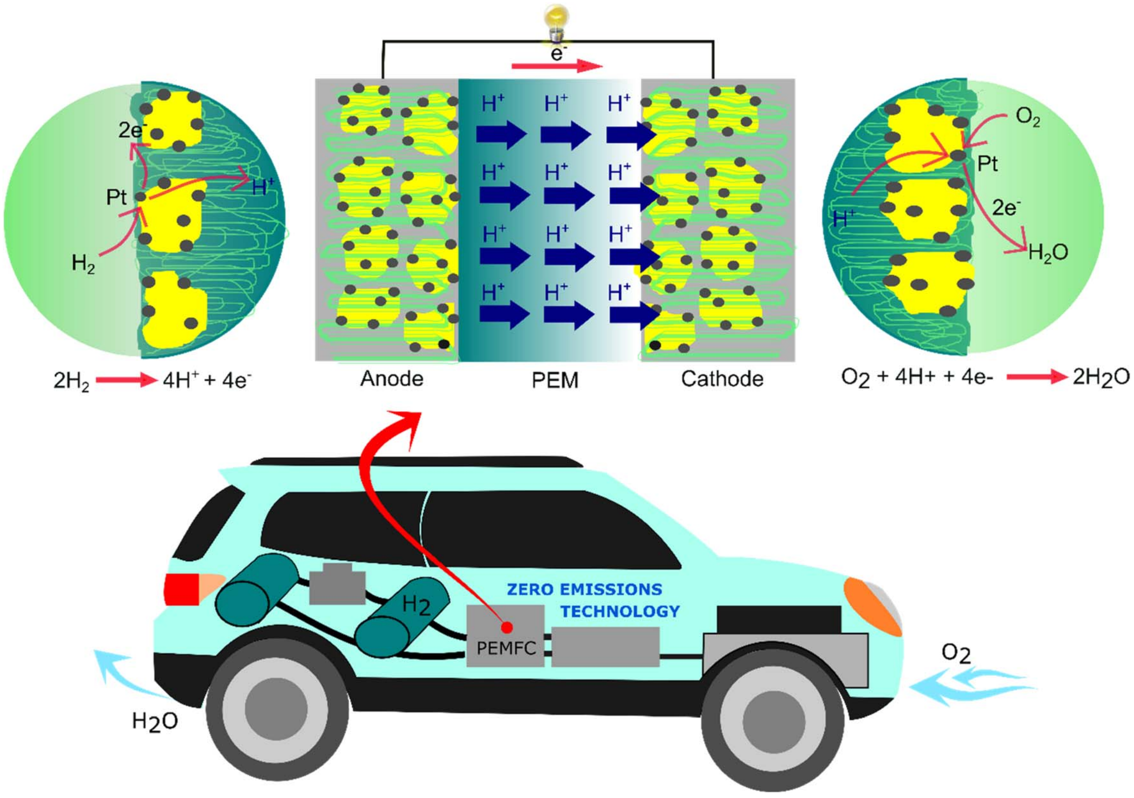

Fig. 1 The illustration of the core mechanism in PEMFCs for vehicle application.

mass transfer resistance.[9] Inefficient processes result in performance losses, especially at high current densities where oxygen diffusion is a limiting factor.[10] Optimizing the structure and arrangement of the catalyst layer is necessary to improve the performance of PEMFCs and cost reductions.

Recent studies compiled on the design of ordered catalyst layers have demonstrated promising outcomes in overcoming the limitations of conventional layers.[11–13] In contrast to chaotic structures, ordered catalyst layers have a properly structured structure that facilitates the efficient transit of electrons and protons. It has been demonstrated that ordered catalyst layers achieve a higher electrochemical surface area (ECSA),[14] improved catalyst utilization,[15] enhanced mass transport,[16] and better water management[17] and deliver superior power densities.[18,19]

The primary goal of this review is to establish theoretical underpinnings for ordered catalyst layers in PEMFCs that have not yet been established. The knowledge gained from this will be utilized in order to optimize the catalyst layer in the PEMFCs. Moreover, the implications of switching from conventional catalyst layers (CCLs) to ordered catalyst layers (OCLs) in PEMFC applications were discussed. These implications included important aspects such as mass transfer, reaction rates, platinum utilization, water management, and the generation of electricity, all of which are essential for interpreting the performance of PEMFCs. Modelling, manufacturing scalability, imaginative structural designs, and the distribution of discoveries are some of the future approaches that will be pursued. These directions will provide insights into improving the performance and practicality of PEMFCs.

2. Catalyst layers: origin and advancement

The technology behind fuel cells has experienced major technological advancements over the course of the previous two centuries. Some of the most important developments that have paved the way for their expansion and use are catalyst layers. In order to overcome issues with efficiency, cost, and scalability, catalyst layer research has been an integral part of PEMFC technology evolution. Improving catalyst layers is a key area for future research into PEMFCs, which could lead to their widespread use as a green energy source. Fig. 2 illustrates the time frame considering fuel cell origin and catalyst development.

The principle of electrochemical energy conversion was initially demonstrated by Sir Humphry Davy in the 1800s through his investigations on electricity produced from chemical processes.[20] Later, in 1839, Sir William Grove created the “gas battery”, which used hydrogen and oxygen to make water and energy. Despite its simplicity, Grove's work provided the foundational electrochemical principles that underlie contemporary fuel cells.[21] Throughout this period, the catalyst layer crucial for enhancing reactions and efficiency remained unrefined.

At the beginning of the 20th century, Francis Thomas Bacon developed alkaline fuel cells (AFCs), which were the initial

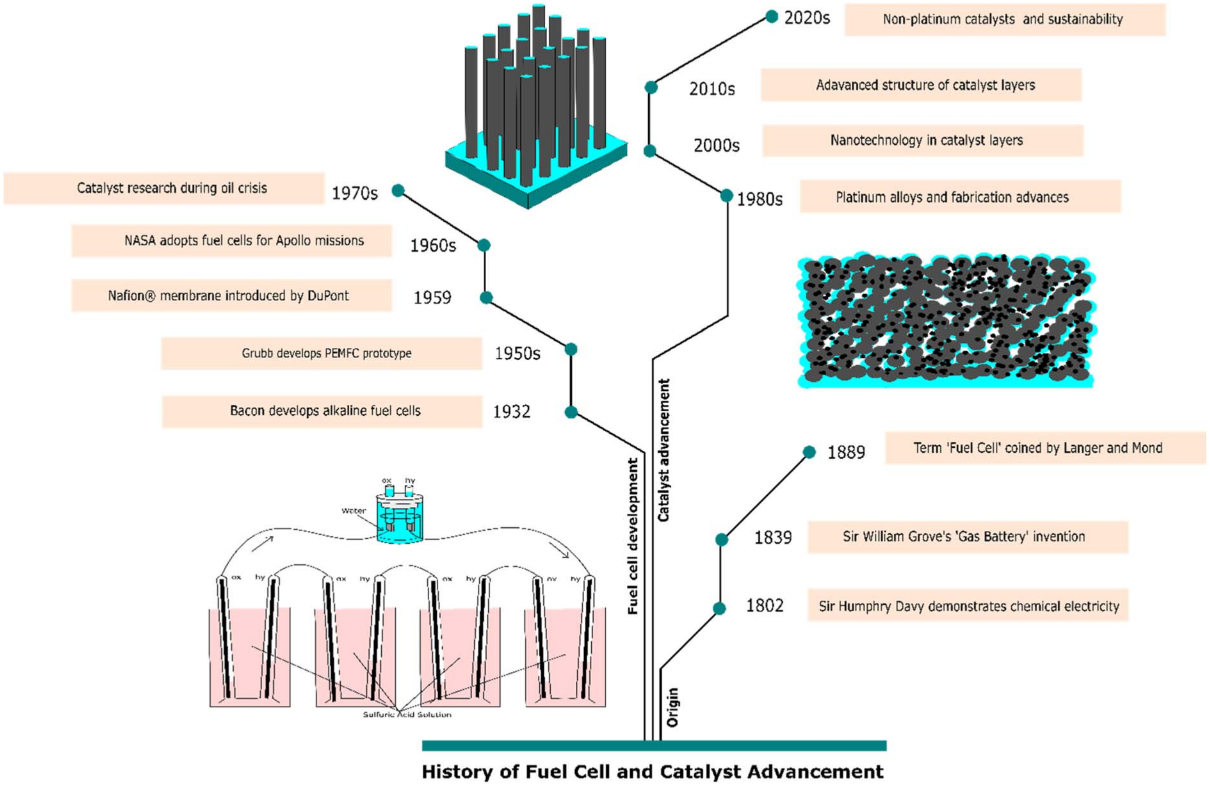

Fig. 2 The time frame of fuel cell development starting with its origin starting with Sir Humphry Davy, Sir William Grove, and Langer and Mond, continued with notable milestone applications such as alkaline fuel cells, PEMFCs, the Nafion membrane and Apollo mission, and recent development of catalysts including the oil crisis period, platinum alloy and fabrication methods, nanotechnology approach, and non-platinum catalyst development.

devices to use porous nickel electrodes for gas diffusion.[22] The utilization of structured electrodes to improve the efficiency of catalysts was one of the first applications of this technology. By the year 1950, Willard Grubb, working for General Electric, had developed the first proton exchange membrane fuel cell (PEMFC). This fuel cell utilized platinum as a catalyst on sulfonated polystyrene membranes.[22] These early catalyst layers, despite their effectiveness, were plagued by high platinum loading, which hindered their potential to be economically viable.

In the late 1950s, DuPont made a big step forward when they released Nafion®.[23] Enhanced proton conductivity and improved catalyst layer integration were both made possible by using this membrane composed of perfluorosulfonic acid. Despite these developments, the expensive cost of platinum in catalyst layers and its limited availability continued to be a significant obstacle to the general use of the technology.

NASA's adoption of fuel cells for the Apollo program in the 1960s was highly significant for PEMFCs.[24] During this time, platinum was deposited on porous surfaces to provide catalyst layers that ensured proper reactant access and reaction kinetics. To improve the performance and longevity of platinum catalysts, which are incredibly resistant to temperature changes and chemical oxidation, General Electric improved these designs for use in aerospace applications.[25] On the other hand, the reliance on very high platinum loading brought to light the requirement for designs that are both more cost-effective and efficient.

The oil crises of the 1970s prompted substantial research into fuel cells as alternative energy solutions.[26] The primary objective of researchers during this decade was to enhance mass transport and decrease platinum usage. A standard approach of integrating porous carbon-supported platinum catalysts has been established, enabling improved catalyst distribution and utilization. This marked the beginning of a move from designs that were completely experimental to PEMFC layouts that were more practical.

The introduction of platinum-alloy catalysts in the 1980s, such as Pt–Co and Pt–Ni, which improved the kinetics of the oxygen reduction reaction (ORR), led to a substantial advancement in the development of catalyst layers throughout the decade.[27] These alloys decreased the amount of platinum loading while maintaining a high level of catalytic activity, which paved the way for more cost-effective designs of PEMFCs. Additionally, the utilization of methods such as screen printing and spraying made it possible to carry out the precise placement of catalyst layers onto gas diffusion layers.[28] Consequently, this resulted in improved cell efficiency and performance, since it ensured a uniform distribution of the catalyst and improved accessibility to the reactants.

The commercialization of Proton Exchange Membrane Fuel Cells (PEMFCs) commenced in the early 1990s, especially for automotive applications. For example, the initial fuel cell buses have been introduced by over 13 firms, including notable names such as Volvo, Daimler-Chrysler, and Toyota, among others, which have developed their own fuel cell bus prototypes.[29]

In the 2000s, breakthroughs in nanostructured catalyst layers were achieved. This method reduced resistance and improved overall system efficiency. There is a huge growth in interest in the development and use of micro- and nanometer-scale materials with hollow interiors as solid catalysts.[30] During that time, the understanding of synthetic approaches for producing such structures is limited. The study advancement focused mostly on the controlling of morphologies in different types of materials.

During the 2010s, organized catalyst layers emerged as the primary focus for researchers aiming to enhance PEMFC performance. For example, the development of double-layer catalyst morphologies has been observed to improve mass transport and minimize platinum loading while maintaining high power outputs. Additionally, the effect of Pt-loading on the number of active sites and the thickness of the catalyst layer has been assessed. This has resulted in a significant impact on mass transfer and water management during dynamic processes in PEMFCs.[31]

During the 2020s, investigations into non-platinum catalysts accelerated to decrease expenses and improve the sustainability of PEMFCs. Catalysts utilizing iron–nitrogen doped carbons and manganese–nitrogen complexes have demonstrated potential in attaining performance levels like platinum-based systems. Reports indicate that the high-temperature pyrolyzed FeN_x/C catalyst, synthesized from poly-*m*-phenylenediamine (PmPDA-FeN_x/C), exhibits significant ORR activity (11.5 A g^{-1} at 0.80 V *vs.* RHE) and minimal H_2O_2 yield (<1%) under acidic conditions.[32] A different study indicated that electrochemical measurements demonstrate that the synthesized Mn–N–C catalyst is comparable to the Fe–N–C catalyst produced *via* the same method and even displays enhanced cycling stability, losing only 20 mV after 10 000 cycles (0.6 to 1.0 V in O_2 saturated electrolyte).[33]

3. Fundamental theories

Ordered catalyst layers, also known as OCLs, provide a structured arrangement of catalytic sites, in which platinum particles are dispersed in a uniform manner. By highlighting the potential of OCLs to improve the efficiency of PEMFCs, the theoretical perspective that was presented demonstrates that it is a promising strategy for the development of future fuel cell technology.

3.1. Mass transport

The diffusion to catalyst sites is a crucial component that influences efficiency. Fick's law[34] is generally applicable to the mathematical characterization of gaseous diffusion properties in a catalyst layer, as described by the equation:[35]

$$\varepsilon \frac{\partial C_g}{\partial t} = D_{\mathrm{g}}^{\mathrm{eff}} \nabla^2 C_g$$

where ε represents the porosity of the catalyst, C_g denotes the concentration of the gaseous species g, and $D_{\mathrm{g}}^{\mathrm{eff}}$ refers to the effective diffusion coefficient of the gas. In a conventional catalyst layer, the effective diffusion coefficient $D_{\mathrm{g}}^{\mathrm{eff}}$ is adjusted for tortuosity and porosity by applying the Bruggeman correlation.[36] The effective diffusion coefficient in the porous media of PEM fuel cells is more accurately described by percolation theory,[37] as defined using the equations:

$$D_{\mathrm{g}}^{\mathrm{eff}} = f(\varepsilon) x D_{\mathrm{g}}^{\mathrm{i}}$$

$$f(\varepsilon) = \varepsilon \left(\frac{\varepsilon - \varepsilon_{\mathrm{p}}}{1 - \varepsilon_{\mathrm{p}}} \right)^{\alpha}, \quad \alpha = \begin{cases} 0.521 \text{ in-plane} \\ 0.785 \text{ throgh plane} \end{cases}$$

$D_{\mathrm{g}}^{\mathrm{i}}$ represents the bulk diffusion coefficient, while ε defines the porosity of the layer. This equation considers that the random structure of CCLs considerably reduces D_{eff}, making the transfer of oxygen inefficient, especially at high current densities. By enhancing the uniformity and decreasing the tortuosity of the ionomer, this approach facilitates the distribution and prevents the disproportionate merging of ionomer films.[38] The Bruggeman correlation, applying exponents of 1.5 (parameters related to the tortuosity factor), has been frequently used in the modeling of PEM fuel cells.[35,39,40] However, it is suggested that this exponent significantly exceeds that of the carbon fiber-based catalyst layer materials in PEM fuel cells. Furthermore, it has been noted that the pore structure influences the non-uniform distribution of water saturation,[41] suggesting that the assumption may be imperfect, and the exponent could range between 2.0 and 5.0, even with varying values.[42] On the flip side, OCLs overcome these constraints by establishing a highly structured framework. The systematic arrangement of Pt particles reduces requirements for tortuosity adjustments, facilitating enhanced oxygen diffusion.[43,44]

The increase in oxygen diffusion in OCLs can also be assigned to a reduction in Knudsen diffusion limitations, since the aligned pores in OCLs allow for more efficient molecular and Knudsen diffusion than in CCLs. It has been pointed out that Knudsen diffusion had a significant impact on the relative diffusion coefficient.[44,46] It has been reported that for media with pore dimensions ranging from 2 to 50 nm,[47] Knudsen diffusion is the primary transport mode developed from gas molecules interacting with the pore walls rather than Brownian

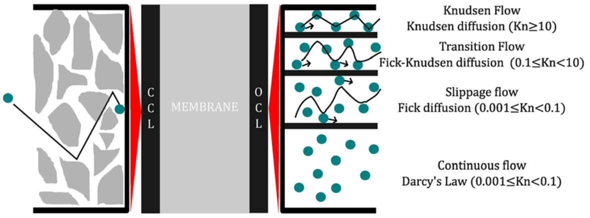

Fig. 3 Gas flow patterns in a porous medium correlated with the Knudsen number[45] with a comparative structure.

motion or intramolecular collision.[48] Fig. 3 presents gas flow patterns in a porous medium correlated with the Knudsen number. It should be noted that increasing the pore size results in a reduction in the Knudsen collision effect, so molecules collide more frequently with the pore walls and shift the diffusion mechanism from Knudsen to Fick—where Fick diffusion generally occurs in large pores (macrospores) and Knudsen diffusion dominates in small pores (microspores)—so that when the pore size reaches 50 nm, Fick diffusion characteristics begin to appear.[45] Theoretical analysis of these diffusion mechanisms confirms that OCLs provide a more efficient transport pathway, lowering oxygen concentration gradients and improving ORR performance. The Knudsen diffusion coefficient is determined by the gas species and pore diameter, and it is expressed as[49]

$$D_{i,\mathrm{Kn}} = \frac{d_\mathrm{p}}{3}\sqrt{\frac{8RT}{\pi M_i}}$$

where d_p defines the diameter of pores, R is the molar gas constant, and M_i is the molar mass of gas species i.

The effective diffusion coefficient, incorporating both bulk diffusion and Knudsen diffusion, is defined using the following equation:[50–52]

$$\frac{1}{D_\mathrm{eff}} = \left(\frac{1}{D_\mathrm{b}} + \frac{1}{D_\mathrm{k}}\right) x f(\varepsilon)$$

where Deff defines the diffusion coefficient in a single cylindrical pore, D_b denotes the bulk diffusion coefficient, D_k is the Knudsen diffusion coefficient, and ε represents the porosity of the catalyst.

The improved mass transfer characteristics of OCLs have been validated in multiple investigations. For example, an oriented Pt/CNT-based MEA demonstrates superior performance compared to both Pt/C and non-oriented Pt/CNT-based MEAs. This is attributed to the superhydrophobicity of the oriented Pt/CNT film, which effectively prevents water accumulation at the cathode in the mass transfer-controlled region (high current density). In contrast, the MEAs with non-oriented Pt/CNTs and Pt/C exhibit diminished performance primarily due to electrode submersion and the resultant mass transport challenges.[53]

The polarization performance experiments confirmed that the Pt/CSCNT MEA surpasses the E-TEK MEA in the high current density region.[54] This outcome was revealed using the calculation of cell resistance using the *iR* interrupt approach and the contributions of H_2 crossover current at various overpotentials relative to current density. As the current density increases, the changes become more pronounced. This alteration can be attributed to the internal mass transfer overpotential in the context of the E-TEK MEA.

Further investigations indicated that an ordered catalyst layer, constructed from macroscopic pores created by the removal of the colloidal template, could enhance mass transfer. The current density for the traditional MEA was measured at 235 mA cm^{-2}, while the ordered structure exhibited a current density of 440 mA cm^{-2}, representing an increase of 185% under identical conditions.[55] This report indicates that the performances of PEMFCs in the low-current range are rather comparable. The feature is not significant because conditions are in the charge transfer-controlled region. However, in the high-current region, the superior outcome is related to the structural advantages.

A theoretical investigation was conducted to analyze the effect of isotropy (order *versus* dispersion) on the effective diffusion coefficient (D_eff) of the PEMFC catalyst layer.[56] Finite volume and simulated annealing methods were used to model the structural transition from aligned bars to random (monodispersed). The results showed that the ordered structure (low isotropy, $I_{xy} = 0$) enhances mass transport when diffusion is parallel to the bars, reducing the oxygen barrier. At pore surface fraction ≥50%, D_eff reaches a maximum of 6.20×10^{-8} m^2 s^{-1} (dominant pore diffusion). However, increasing isotropy ($I^{xy} \rightarrow 1$) decreases D_eff exponentially, especially when the pore fraction is <50%, approaching the ionomer diffusion value ($D_{\mathrm{O_2},\mathrm{Agg}}$). This research deduced that the anisotropic catalyst layer design with pore dominance (≥50%) improves D_eff and cell performance, while the random structure with high isotropy reduces the mass transport efficiency. These findings form the basis for optimizing PEMFC catalyst design for maximum performance.

Other experimental results show that the semi-ordered CL's pressure-independent oxygen transport resistance is reduced by more than 35% at a Pt loading of 0.05 mg$_\mathrm{Pt}$ cm^{-2} and almost 50% at 0.1 mg$_\mathrm{Pt}$ cm^{-2} compared with a conventional CL.[57] This indicates that the vertical transport pathway formed by the micro-array contributes to accelerating the oxygen diffusion to the active sites of the catalyst, thereby improving the efficiency of the oxygen reduction reaction (ORR). Furthermore, in this report, multiphysics modeling results confirm that the presence of semi-ordered structures in the CL extends the operating region with limited mass transport and increases the peak power density (PPD) by 24%, reaching 926 mW cm^{-2} at a Pt loading of 0.1 mg cm^{-2}. These findings confirm that the semi-ordered design not only overcomes the Knudsen diffusion barrier in conventional CLs but also enhances Pt utilization and proton transport without causing a significant increase in ohmic resistance, making it a potential solution for lowering the Pt loading without compromising the performance of PEMFCs.

3.2. Reaction rates

The reaction kinetics are vital to the overall performance of PEMFCs. In CCLs, platinum particles tend to get agglomerated, decreasing the surface area that is available for the reaction.[58] This results in the deterioration of the catalyst and a decline in catalytic activity.[58] The non-uniform distribution and considerable particle size of Pt have been observed to contribute to an inhomogeneous chemical composition among alloy nanoparticles, therefore reducing the catalyst's activity. The carbon support could be converted to CO_2, resulting in the loss of Pt in the electrode.[58] Supported carbon particles with platinum are vulnerable to degradation during fuel starvation, while the oxidation of carbon is facilitated by the presence of platinum. It should be underlined that as the Pt content increases, the corrosion of Pt/C becomes more severe. As Pt accelerates the next oxidation of CO_{surf} to CO_2, a deficiency in Pt slows down this process.[58–60] The reactions follow as:[58]

$$C + H_2O \rightarrow CO_{surf} + 2H^+ + 2e^-;\ CO_{surf} + H_2O \rightarrow CO_2 + 2H^+ + 2e^-$$

$$Pt + H_2O \rightarrow Pt\text{–}O + 2H^+ + 2e^-;\ CO_{surf} + Pt\text{–}O \rightarrow CO_2 + Pt$$

The kinetics of electrochemical reactions in catalysts can be characterized using the Butler–Volmer equation and the Tafel equation. Fig. 4 explains the regions considered Buttler–Volmer and Tafel regions. The Butler–Volmer equation comprises the total of both forward and backward reactions in a redox couple following the formula as:[61]

$$i = i_{\text{cathode}} + i_{\text{anode}} = i_0\left\{-e^{-\frac{\alpha nF\eta}{RT}} + e^{-\frac{(1-\alpha)nF\eta}{RT}}\right\}$$

where i represent the total current (forward + backward), i_0 defines the exchange current density, α is the transfer coefficient, n denotes the number of electrons exchanged during the oxidation/reduction of a single molecule, and η denotes the overpotential. F is Faraday's constant, R is the universal gas constant, and T is the absolute temperature.

The modified Butler–Volmer equation, incorporating Pt-oxide-coverage-dependent kinetics,[62] is employed to characterize the oxygen reduction reaction (ORR) in the cathode catalyst layers (CLs).[63] Here, θ_{PtO} denotes the oxide coverage, a potential-dependent variable as expressed in the subsequent equation, and ω represents the coverage-dependent adsorption rate, and the reaction order of the ORR (γ_c) in the cathode is

$$i_{\text{cathode}} = A_c i_{0,c}^{\text{ref}}(1-\theta_{\text{PtO}})\left(\frac{C_{\text{O}_2\text{Pt}}}{C_{0,\text{ORR}}^{\text{ref}}}\right)^{\gamma_c}\exp\left(-\frac{\alpha_c}{RT}F\eta_C - \frac{\omega\theta_{\text{PtO}}}{RT}\right)$$

where η_c represents the cathode overpotential, $C_{0,\text{ORR}}^{\text{ref}}$ denotes the reference exchange current density for the oxygen reduction reaction (ORR), and α_c signifies the transfer coefficient of the ORR.

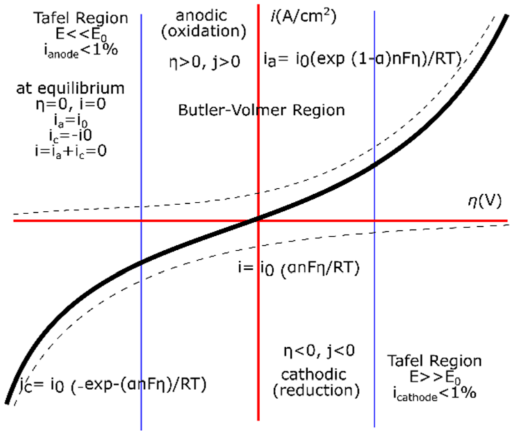

Fig. 4 Current–potential curves of the Buttler–Vormer equation and its relationship to the Tafel region.

A simplified Butler–Volmer equation was provided for the computation of the hydrogen oxidation reaction (HOR) rate in the anode catalyst layers (CLs).[63]

$$i_{\text{anode}} = A_a i_{0,a}^{\text{ref}}\left(\frac{C_{\text{H}_2\text{a}}}{C_{0,\text{HOR}}^{\text{ref}}}\right)^{\gamma_a}\exp\left(\frac{\alpha_a}{RT}F\eta_a\right)$$

where η_a denotes the anode overpotential, $C_{0,\text{HOR}}^{\text{ref}}$ represents the reference exchange current density for the hydrogen oxidation reaction (HOR), and α_a signifies the transfer coefficient of the HOR.

The active specific surface area (A) of cathode and anode CLs could be expressed using Pt loading,[63]

$$A = \frac{Em_{\text{pt}}}{\delta_{\text{CL}}} = \frac{3m_{\text{pt}}}{\rho_{\text{pt}}r_{\text{pt}}\delta_{\text{CL}}}$$

where m_{Pt} represents the platinum loading of the cathode or anode catalyst layers (CLs), ρ_{Pt} and r_{Pt} denote the density and particle radius of the platinum catalyst, and δ_{CL} indicates the thickness of the cathode or anode CLs.

Conversely, the Tafel formula facilitates the acquisition of information regarding activity by utilizing the Tafel slope to exchange current density and mechanism:[64–66]

$$\eta = a + b\log i$$

where η is the overpotential in mV, a is the Tafel intercept, representing the overpotential (η) when $\log i = 0$, i is the current density in mA cm^{-2}, and b is the Tafel slope in mV dec^{-1}. The primary distinction is that the Tafel equation is a simplified equation that is applicable when single reactions are significant. Fig. 4 illustrates the Butler–Vormer and Tafel regions.

The availability of active sites for the reaction is directly correlated with the exchange current density i_0, while I_0 is reduced due to the agglomeration of Pt particles. The overpotential is increased because of the restricted availability of Pt sites. The Pt particles are uniformly disseminated on aligned supports in OCLs, which optimizes the exposure of Pt sites to the reacting species. This leads to a reduction in overpotentials and an increase in the exchange current density i_0, as the uniform distribution of Pt enables the efficient access of reactants.

Modelling studies indicate that OCLs can diminish overpotentials relative to CCLs, as the ordered structure provides a higher proportion of Pt sites that are actively engaged in the ORR.[67–69] The decrease in overpotential results in accelerated response rates and enhanced power densities, significantly enhancing the fuel cell's performance.

3.3. Pt utilization

The efficiency of platinum use is a critical determinant of the economic viability and value of proton exchange membrane fuel cells (PEMFCs). In CCLs, Pt particles are distributed randomly, frequently causing specific catalytic sites to be inaccessible, hence decreasing total usage. Conversely, OCLs are engineered to establish a consistent configuration of Pt particles. The structural design and configuration need to be considered to produce an innovative CL architecture that enhances material transport efficiency, hence improving high output power and durability under ultra-low Pt loading.[70]

The investigation of platinum (Pt) utilization and effectiveness factors in polymer electrolyte fuel cells (PEFCs) is essential for overcoming obstacles such as inadequate power densities and high expenses. The high cost and limited availability of platinum, a critical component of catalyst layers in fuel cells, are the primary causes of these challenges. Consequently, the advancement of fuel cell technology is contingent upon the comprehension and enhancement of Pt utilization and its efficacy factor. The operational implications, mathematical frameworks, and definitions of Pt utilization and effectiveness factors have been reported, with an emphasis on the importance of ordered catalysts in optimizing these metrics.[71]

Pt utilization is typically characterized as the ratio of the total surface area of Pt particles to the electrochemically active surface area of Pt that is accessible for reactions. This can be expressed mathematically as:[71]

$$U_{\mathrm{Pt,CL}} = \frac{S_{\mathrm{Pt,CL}}}{S_{\mathrm{Pt,tot}}}$$

where $S_{\mathrm{Pt,CL}}$ denotes the active electrochemical surface area within the catalyst layer and $S_{\mathrm{Pt,tot}}$ is the total surface area of Pt particles. The effectiveness of Pt nanoparticles in the oxygen reduction reaction (ORR) within the fuel cell is determined by this metric. In practice, Pt utilization frequently fails to achieve 100% due to factors such as partial coverage of Pt particles by ionomer coatings, poor electronic connectivity, and non-uniform proton accessibility. For example, the active participation of certain Pt particles in electrochemical reactions may be restricted or prevented by ionomer isolation or encapsulation. Furthermore, the utilization of reactants, particularly oxygen, is further diminished under operational conditions due to transport constraints. The results show significant uncertainty and inconsistent standards for assessing Pt usage across different experimental trials. The total charge transferred upon hydrogen adsorption may unintentionally involve non-wetted inactive catalyst surface area or include the catalytically inert substrate surface because of the so-called spillover effect.[72]

The effectiveness factor (Γ_{CCL}) provides a more sophisticated knowledge of Pt consumption. It compares the actual rate of current conversion in a given catalyst layer to the optimal rate obtainable if all Pt atoms were uniformly active. The mathematical formulation consists of two main components: statistics and operational elements. This can be expressed as:[71]

$$\Gamma_{\mathrm{CCL}} = \Gamma_{\mathrm{stat}} \cdot \Gamma_{\delta}$$

Γ_{stat} takes into account statistical characteristics such as the surface-to-volume ratio of Pt nanoparticles and spatial inhomogeneities, whereas Γ_{δ} indicates the ratio of real to ideal current densities, which includes transport and reaction rate non-uniformities. The effectiveness factor is especially valuable because it captures the dynamic interplay between structural, material, and operational factors in catalyst performance.

Operational characteristics have a considerable impact on Pt utilization and effectiveness factors. Higher operating temperatures improve proton conductivity and oxygen diffusion, leading to more consistent reaction rates across the catalyst layer. Similarly, increased oxygen partial pressures improve reactant dispersion, hence reducing transport restrictions. The agglomeration radius also has an important effect. Smaller agglomerates have higher effectiveness factors because reactants and protons can more easily enter and react at active areas within the structure. In contrast, bigger agglomerates contain inactive cores, limiting overall effectiveness. Fig. 5 illustrates the degrading mechanism associated with platinum particles on a carbon support in fuel cells comprehensively.[60,73]

It has been studied that the pore configuration of the carbon support and the distribution of the Pt particles can affect the catalyst's performance. Research indicates that accessible porous carbons feature hollow interiors with a greater quantity and size of mesopores compared to conventional porous carbons.[74] The active sites facilitate efficient oxygen transport; however, these regions are constrained in proton transport owing to the lack of a proton-conducting ionomer layer. Conversely, substantial ionomer agglomerates, densely coated on Pt, facilitate proton transport while obstructing the passage of oxygen to the active surface. Consequently, only specific regions of the Pt surface exhibit electrochemical activity, and the ratio of the electrochemically active surface area (ECSA) to the structural surface area of Pt (SPt), referred to as Pt utilization (UPt), serves as an indicator for evaluating electrode efficiency.[75]

It has been reported that the platinum utilization value for electrodes in full-cell systems (less than 0.7) is much lower than that in liquid half-cell systems (which is generally above 0.9). As a result, it is crucial to optimize UPt by making sure that all catalyst particles are accessible to the reactants (protons and oxygen) in a full-cell system in order to have an efficient electrode.[75] The advancement in increasing Pt use has been claimed to be influenced by the production procedure. Research

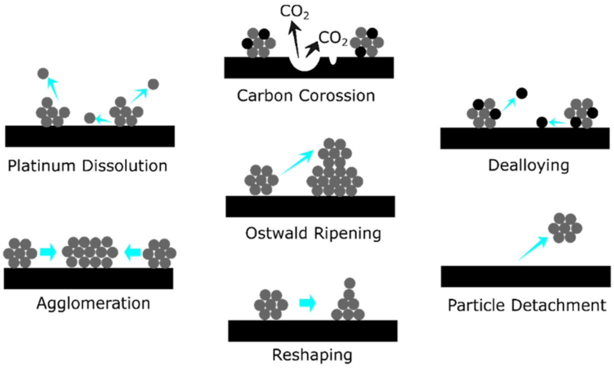

Fig. 5 Illustration of degradation mechanisms for platinum particles on a carbon support in fuel cells.

indicates that manufacturing *via* the spraying approach results in low platinum utilization, hence requiring increased catalyst loading. The performance of the prepared MEAs, produced using spraying and screen-printing methods, was compared, revealing that the screen-printed MEA surpassed the sprayed MEA.[76] The investigation revealed that the electrosprayed catalyst layer in the cathode enhanced Pt consumption from 3.3 to 20 kW g_{Pt}.[77] The electrospinning approach has also been reported to improve Pt use. The electrospinning process achieves an ultralow loading of 0.029 mg_{Pt} cm^{-2} and demonstrates a Pt utilization of 10.5 kW g_{Pt}.[78,79] The integration of these two approaches has been established, yielding a total platinum utilization of 0.076 g_{Pt} kW^{-1} (about 13.2 kW $g_{Pt}{}^{-1}$) with a total Pt MEA loading of only 0.094 mg_{Pt} cm^{-2}.[80]

3.4. Water management

Water management within the CL is a crucial component that considerably influences PEMFC efficiency. An insufficient quantity of water in the CCL results in reduced ionic conductivity and renders the catalyst surface partially exposed, hence contributing to resistive and kinetic cell voltage loss.[81] Conversely, excessive water will block the catalyst surface and limit the transfer of reactant gases, resulting in a decrease in mass transport-related performance.[82] The catalyst layer is seen as a macro-homogeneous layer, allowing for the quantification of the physical structure of the catalyst layer using its porosity. In CCLs, internal pores are random, making it impossible to physically quantify a randomized structure.[83]

The water generated during the ORR can saturate the porous structure of CAL, impeding oxygen routes and resulting in degradation in performance at elevated current densities.[84] The flooding phenomenon is intensified in CAL due to its irregular porosity, which fails to effectively direct liquid water away from reaction sites. In OCLs, the ordered configuration enhances water management by establishing designated pathways for liquid water removal, hence diminishing the risk of floods.[85] Liquid water occupies all the pores between Pt and Nafion-coated VACNTs; the governing equation for oxygen transport in the water subdomain can be expressed as:[86]

$$\nabla \cdot (D_{O_2,w} C_{O_2}) = 0$$

In this equation, $D_{O_2,w}$ is the oxygen diffusivity and C_{O_2} is the oxygen concentration.

In water-related subdomains, oxygen transport follows Fick's law and oxygen diffuses from the air into the GDL. The oxygen concentration at the boundary between the water subdomain and the gas diffusion layer (GDL) is determined using Darcy's law for fluid flow in porous media. Because of the optimization of the structure, OCLs are able to maintain a higher permeability to water than CAL, which results in improved oxygen availability and performance that is maintained throughout extended periods of operation.[87]

Darcy's law governs gas and liquid water two-phase flow in porous media, which depends on permeability. Porous material K_{eff} has effective permeability according to[49]

$$K^{eff} = k_{abs} k_r$$

where k_{abs} is absolute permeability and k_r is relative permeability. K_r is S^3 for liquid and $(1 - S)^3$ for gas.

The phase transition of water between liquid and vapor is characterized by the processes of evaporation and condensation.[89] The sources of condensation and evaporation (S_{ec}) are expressed as a function of decreased saturation (s_{red}),[90] defined using

$$\text{For evaporation} \left(\text{if } p_{H_2O} < p_{sat}\right) : S_{ec} = \frac{k_e a_{lg} S_{red} \left(p_{H_2O} - p_{sat}\right)}{RT}$$

$$\text{For condensation} \left(\text{if } p_{H_2O} > p_{sat}\right) : S_{ec} = \frac{k_e a_{lg} (1 - S_{red}) \left(p_{H_2O} - p_{sat}\right)}{RT}$$

where a_{lg} defines the effective liquid–gas interfacial surface area density scaling factor, p_{H_2O} denotes the pressure of water, p_{sat} refers to the saturation pressure of water, k_e is the rate of water evaporation and k_c is the rate of water condensation.

The adsorption and desorption of water vapor sources (S ad) in the anode and cathode catalyst layers (CLs) are represented as a function of water concentration (λ),[90,91] as follows:

$$\text{For absorption} \left(\text{if } \lambda < \lambda_{eq}\right) : S_{ad} = \frac{k_a}{\delta_{CL} V_m} \left(\lambda_{eq} - \lambda\right)$$

$$\text{For desorption} \left(\text{if } \lambda > \lambda_{eq}\right) : S_{ad} = \frac{k_d}{\delta_{CL} V_m} \left(\lambda_{eq} - \lambda\right)$$

where λ_{eq} denotes the equilibrium water content of the ionomer and k_a and k_d signify the rates of water adsorption and desorption in the catalyst layers (CLs). δ_{CL} represents the thickness of CLs. V_m represents the molar volume of the ionomer.

Fig. 6 illustrates the comparison between a conventional catalyst layer and an ordered catalyst layer on multiscales. A 3D model of an order-structured cathode catalyst layer (CCL) has been constructed under water flooding conditions, featuring a vertically aligned carbon nanotube (VACNT) structure. This model serves as the catalyst support with an ultralow platinum loading of less than 0.1 mg cm^{-2}, which is aligned with the U.S. Department of Energy (DOE) 2020 objective.[86] This experiment indicated that parametric analyses involving the length and spacing of VACNTs and the thickness of Nafion reveal that the VACNT-based CCL exhibits exceptional performance even under conditions of water flooding. Another study used a two-dimensional, two-phase, volume-averaged computational model to evaluate how catalyst layer shape and surface wettability affect liquid water flow in PEM fuel cell cathode catalyst layers (CCLs).The findings indicate that the geometric characteristics of the CCL significantly affect liquid water transport.[83]

3.5. Power output

The effectiveness of OCLs over CAL can be quantitatively assessed by examining the polarization curves, which plot cell

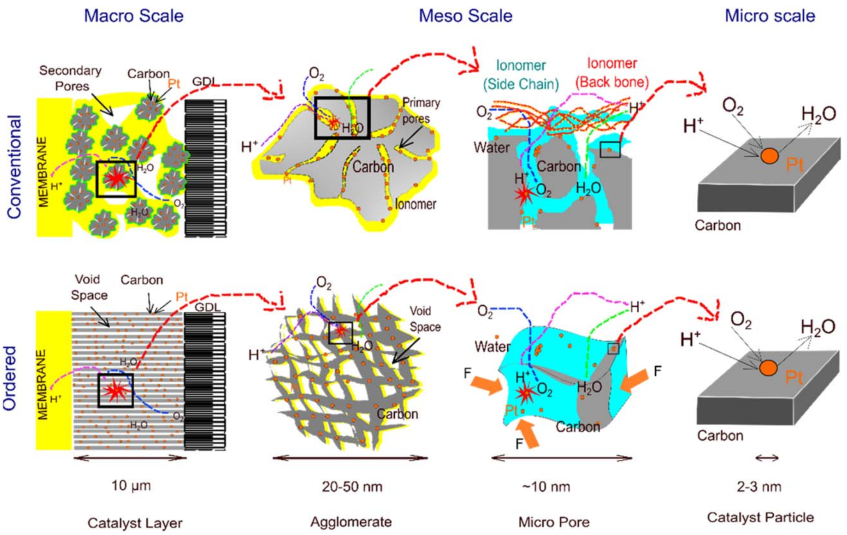

Fig. 6 Illustration of a conventional catalyst layer[88] compared to an ordered catalyst layer on a macroscale, mesoscale, and microscale.

voltage against current density. The superiority of Ordered Catalyst Layers (OCLs) in power density and polarization curves compared to Conventional Catalyst Layers (CCLs) is due to a more organized structure. In CAL, the cell voltage drops rapidly with increasing current density due to combined losses from oxygen diffusion limitations, water flooding, and high ohmic resistance.[92,93] This results in a lower peak power density for CAL, indicating less efficient energy conversion. In contrast, OCL structures exhibit more stable voltage profiles over a broader range of current densities. For instance, it has been reported that the application of Vertically Aligned Carbon Nanotubes (VACNTs) facilitates a more efficient oxygen, proton, and electron transport pathway than in conventional CCLs. Consequently, this structure enables electrochemical reactions to occur more efficiently, thereby increasing power density[86] which is calculated as:

$$P = V \cdot i$$

where V represents the cell voltage and i defines the current density. The OCL cell voltage exhibits greater stability at elevated currents due to reduced ohmic resistance and oxygen transport compared to CCLs.

Reduction of overpotential activation in the polarization curve of the OCL improves polarization curve performance, which is governed by the Butler–Volmer equation. The value of active surface area in OCLs is higher due to the more evenly distributed Pt. This increases the current density, resulting in an enhanced polarization curve.

It has been reported that structured catalysts based on vertically aligned carbon nanotubes (VACNTs) exhibited favorable performance compared to conventional catalysts based on carbon powder. At a much lower platinum (Pt) loading of 35 µg cm^{-2}, the VACNT catalyst was able to achieve a maximum power density of 1.02 W cm^{-2}, almost comparable to the conventional catalyst using a Pt loading of 400 µg cm^{-2} and having a maximum power density of 1.04 W cm^{-2}. In addition, at a cell voltage of 0.6 V, the VACNT catalyst produced a current density of 1.35 A cm^{-2}, only slightly lower than that of the conventional catalyst with 1.52 A cm^{-2}. The efficiency of Pt utilization in the VACNT catalyst was also much higher, with an effectiveness factor reaching 0.36 at a current density of 3 A cm^{-2}, compared to only 0.065 for the conventional catalyst. With this nearly equivalent performance, the VACNT catalyst enables a reduction in Pt usage of up to 90%,[94] Another study found that an ordered catalyst based on CNTs-Pt/TiO$_2$ outperformed a standard Pt/C catalyst in an HT-PEMFC fuel cell test. In the polarization curve test, the CNTs-Pt/TiO$_2$ catalyst with a platinum (Pt) loading of 0.1 mg cm^{-2} achieved a peak power density of 410.6 mW cm^{-2} and a current density at 0.6 V of 0.25 A cm^{-2}. The conventional Pt/C catalyst with a Pt loading of 0.5 mg cm^{-2} provided a higher peak power density of 527.7 mW cm^{-2} and a current density at 0.6 V of 0.56 A cm^{-2}. However, after normalization for Pt loading, the CNTs-Pt/TiO$_2$ catalyst shows considerable advantages. The highest specific power density of Pt mass is 3.60 W mg$_{\text{Pt}}{}^{-1}$, approximately 3.53 times greater than that of the Pt/C catalyst, which is only 1.02 W mg$_{\text{Pt}}{}^{-1}$. The same exists for the specific current density of Pt mass at 0.6 V, with CNTs-Pt/TiO$_2$ achieving 2.24 A mg$_{\text{Pt}}{}^{-1}$, over twice the value of the Pt/C catalyst, which is only 1.10 A mg$_{\text{Pt}}{}^{-1}$.[95]

It has also been reported that TiO$_2$ nanowire array-based regular structured catalysts applied using the ultrasonic spraying approach outperformed conventional catalysts in polarization curve and power density tests. The regular catalyst (CO-MEA) with 0.21 mg cm^{-2} platinum loading generated a peak power density of 539.1 mW cm^{-2}, 37% higher than that of the conventional catalyst (MEA2) with the same platinum loading, which only reached 398.2 mW cm^{-2}. At 0.6 V, the CO-MEA produced 819.57 mA cm^{-2}, significantly greater than MEA2's 552.74 mA cm^{-2}. The CO-MEA had a current density of 1283.67 mA cm^{-2} and an output power of 511.40 mW cm^{-2} at 0.4 V, while MEA2 had 967.56 mA cm^{-2} and 386.65 mW cm^{-2}. The advantage comes from CO-MEA's superior three-phase mass

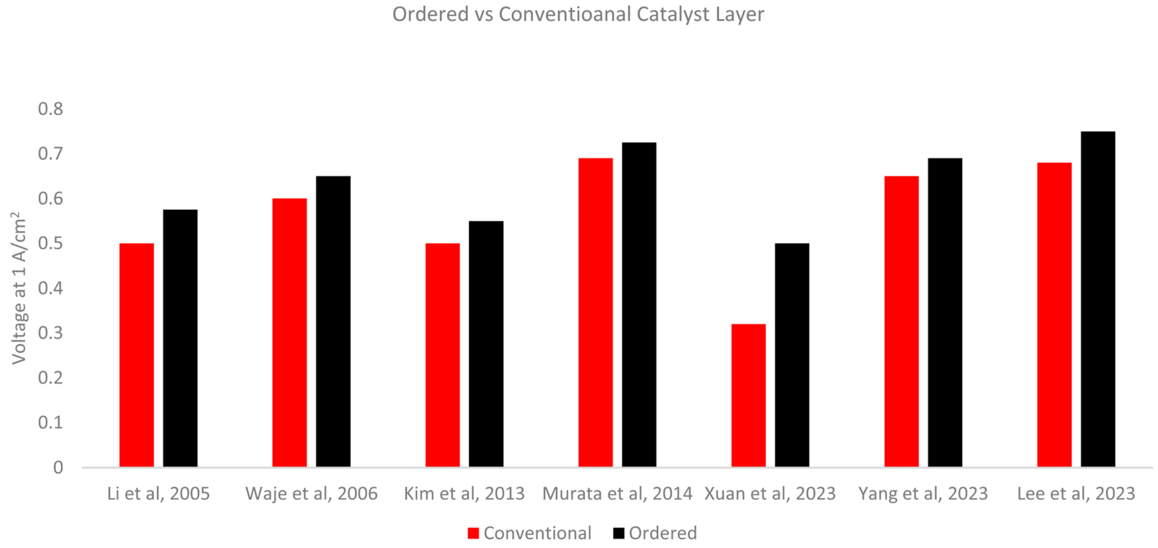

Fig. 7 Comparative results of voltage between ordered *versus* conventional catalyst layers.

transfer channel, which provides a larger active area for electrochemical processes while also optimizing reaction water removal. Thus, this ordered catalyst structure considerably enhances MEA efficiency and performance when compared to traditional catalysts.[96]

Fig. 7 shows comparable voltage at 1 A cm^{-2} between ordered *versus* conventional catalyst layers. Based on the data, the use of Ordered Catalyst Layers (OCLs) increases the average voltage by 0.071 V compared to Conventional Catalyst Layers (CCLs) at a current of 1 A cm^{-2}, equivalent to a power increase of 13.5%. The study by Xuan *et al.* (2023) showed the highest increase (0.180 V), while Murata *et al.* (2014) showed the lowest increase (0.035 V).[97] High variability (standard deviation ≈ 0.048 V) suggests additional factors, such as the material or fabrication, that affect OCL performance. Overall, OCLs consistently improve PEMFC efficiency, but design optimization is needed to reduce the disparity in results between studies.

Table 1 compares the PEMFC-ordered catalyst layer (OCL) *versus* the conventional catalyst layer (CCL) in terms of each key parameter, including mass transport, reaction rate, platinum utilization, water management, and power output. The formula correlated with each parameter has also been addressed and intertwined with the effect for the ordered catalyst layer.

4. Future research direction, potential breakthroughs, and remaining obstacles

4.1. Modelling and simulation approaches

Simulation or modelling helps understand the effect of organized structures in PEMFCs including flow field configuration,[98–100] gas diffusion layers,[101–103] catalyst layers,[104–106] and membranes.[107–109] However, in the case of the catalyst layer in a fuel cell, simulation or modelling has the issue of simulating the physical surroundings of the object. Several models have previously been reported based on the research objectives related to cell performance, including the influence of geometric structure parameters of CCLs,[110] a one-dimensional model of OCLs,[67] a modified agglomerate model,[68] the influence of spacing between nanoelectrodes and catalyst layer thickness,[111] and a multiscale model to investigate mass transport characteristics integrated into a two-dimensional, two-phase cell-scale model.[63] Key aspects that are considered for fuel cell characterization need to be investigated to justify the superiority of ordered catalyst layers compiled in Fig. 8.

Table 2 presents a compilation of equations from a recent paper concerning the optimal order-structured cathode catalyst layer linked to a three-dimensional (3D) two-phase macroscopic PEMFC model. This methodology facilitates the numerical optimization of three-phase components within the order-structured cathode catalyst layer. A two-phase 3D numerical model is used in this study to improve the triple-phase components of the ordered catalyst structure. This model considers the ordered structure of vertical carbon nanowires, ionomers, and water films to be major factors in oxygen and proton transfer. The impact of water accumulation on oxygen transport, which is frequently overlooked in other ordered catalyst models, has also been considered. By including all these crucial impacts, the simulation becomes more realistic and useful for practical design. This study found that the best combination is Pt loading 0.15 mg cm^{-2}, carbon loading 1.0 mg cm^{-2}, and ionomer volume fraction 0.2, resulting in a maximum power of 1158 W cm^{-2}. The equation in this work considers the impacts of oxygen resistance in each transport phase (water films, ionomers, and carbon pores), resulting in more accurate predictions than standard empirical formulations.[69]

The research proposes a multiscale model for analyzing oxygen transport properties, combining a macroscopic mass movement framework with a detailed local oxygen sub-model

Table 1 Comparison of Ordered Catalyst Layers (OCLs) *vs.* Conventional Catalyst Layers (CCLs) in PEMFCs

Parameter	Ordered catalyst layer (OCL)	Conventional catalyst layer (CCL)	Supporting formulae
Mass transport	The ordered structure reduces tortuosity and diffusion barriers	Random pores increase tortuosity	Modified Fick's law
	Low gas diffusion resistance due to linear flow	High diffusion resistance, especially during flooding	$D_{\text{eff}} = D\cdot\frac{\varepsilon}{\tau}$
	Knudsen diffusion is minimal because the pores are large and straight	Knudsen diffusion is significant due to the small pores	OCL: decreasing τ causes D_{eff} to increase
Reaction rate	The active surface area (A_v) is higher due to the even distribution of Pt in the regular structure	A_v is low due to agglomeration of Pt	Butler–Volmer equation $i = i_0\left(\frac{C_{O_2}}{C_{O_2}}\right)^{\gamma}\exp\left(\frac{\alpha F\eta}{RT}\right)$
	The active surface area of Pt is more exposed	The reaction is hampered by the uneven accessibility of Pt	OCL: increasing C_{O_2} causes i to increase
Platinum utilization	High Pt utilization due to optimal dispersion	Pt utilization is low because Pt particles are embedded in a random carbon matrix	Effective surface area $A_v = \frac{m_{\text{Pt}}\cdot A_s}{V_{\text{Pt-Nafion}}}$ OCL: A_v is increasing due to the ordered structure
Water management	Regular pores facilitate water drainage, reducing the risk of flooding	Water gets trapped in random pores, increasing the risk of flooding	Relative permeability $K_{\text{eff}} = K_{\text{abs}}\cdot K_r$
	A thin water layer increases the diffusion of O_2	O_2 diffusion is inhibited at saturation	OCL:K_r is increasing due to the regular hydrophilic structure
Power output	High power output	Lower power output, requiring higher Pt loading for similar performance	Cell power $P = E_{\text{cell}}\cdot i$ OCL: i is higher at the same voltage due to lower mass resistance and higher Pt utilization

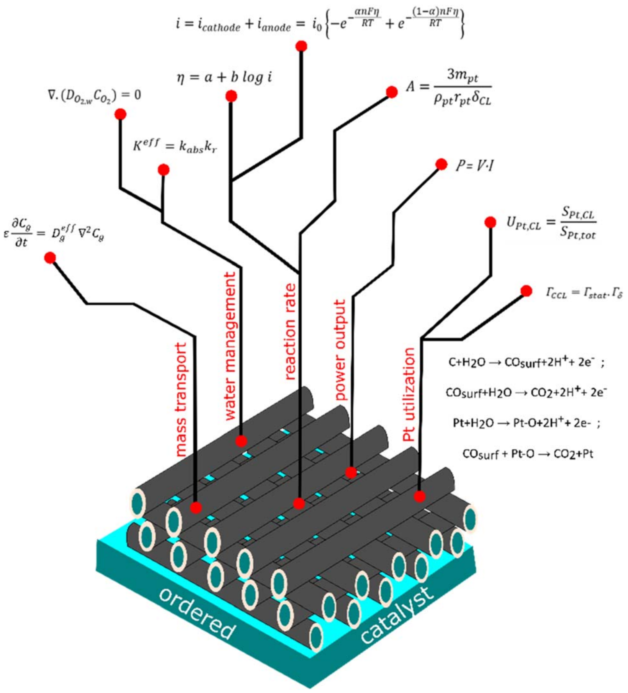

Fig. 8 The illustration of fundamental equations that manage ordered catalyst layer structures considering their aspects.

has been reported.[63] A key aspect of this work is the use of the Langmuir adsorption equation to explain oxygen transport at the Ionomer–Pt interface, which allows for reliable characterization of local oxygen resistance, particularly at low Pt loading. In this work, a Langmuir adsorption equation defined as oxygen adsorption on the Pt surface is used to investigate interfacial resistances. Furthermore, this work presents a logarithmic normalized oxygen transport resistance (OTR) approach for separating and analysing oxygen transport resistance in limiting and non-limited current situations. This method addresses the limitations of traditional limiting current methods, which frequently overlook critical aspects such as operating voltage and oxygen concentration distribution. In this work, the local oxygen transport defines the mass transit of oxygen molecules from bulk pores to the platinum surface. The transport processes encompass five distinct steps. Table 3 compiles the region and elaboration of local oxygen transport.

These results reveal that ordered catalyst layers such as 3D ordered hierarchical porous (3DOHP)[63] and VACNT[69] outperform traditional CLs due to minimal oxygen transport resistance, lower tortuosity, and excellent Pt utilization, particularly at low Pt loading. It should be noted that the current PEMFC modelling with various structural designs (nanofiber, aligned, and VACNT) is still limited compared to the existing experiment sections including nanofiber, aligned, VACNT, coaxial nanowire electrode, orthogonal, nanosheet, grooved, and inverse opal (these structure would be discussed in the following section, remarkable structures), so there are opportunities for discovery and innovation perspectives for mathematicians, computer scientists or other researchers who are engaged in simulation or

Table 2 Governed equations in an ordered catalyst layer model[69]

Aspects	Equations
Mass conservation equation	Catalyst layers are governed by the mass equation following $\frac{\partial(\varepsilon\rho)}{\partial t}+\nabla\cdot(\varepsilon\rho\vec{u})=S_{\mathrm{m}}$, for $S_{\mathrm{m}}\mathrm{anode}=-\frac{M_{\mathrm{H_2}}}{2F}i_{\mathrm{anode}}$ and for $S_{\mathrm{m}}\mathrm{cathode}=-\frac{M_{\mathrm{O_2}}}{4F}i_{\mathrm{cathode}}+\frac{M_{\mathrm{H_2O}}}{2F}i_{\mathrm{cathode}}$ where i represents current density (A m^{-3}), ρ is density (kg m^{-3}), t is time (s), u is momentum, M is molecular weight (kg kmol^{-1}), and F is the faraday constant, 96 485C mol^{-1}
Energy conservation equation	$\frac{\partial(\varepsilon\rho c_{\mathrm{p}}T)}{\partial t}+\nabla\cdot(\varepsilon\rho c_{\mathrm{p}}\vec{u}T)=\nabla\cdot(k^{\mathrm{eff}}\nabla T)+S_{\mathrm{T}}$ S_{T} is mainly related to ohmic resistance, enthalpy change from water evaporation or condensation, and energy released by electrochemical reactions For $S_{\mathrm{T}}\mathrm{anode}=i_{\mathrm{a}}\left(\eta_{\mathrm{anode}}-\frac{T\Delta S_{\mathrm{anode}}}{2F}\right)+\sigma_{\mathrm{e}}^{\mathrm{eff}}\lvert\nabla\varphi_{\mathrm{e}}\rvert^{2}+\sigma_{\mathrm{ion}}^{\mathrm{eff}}\lvert\nabla\varphi_{\mathrm{e}}\rvert^{2}+S_{1}h_{1}$ and $S_{\mathrm{T}}\mathrm{cathode}=i_{\mathrm{a}}\left(-\eta_{\mathrm{cathode}}-\frac{T\Delta S_{\mathrm{cathode}}}{2F}\right)+\sigma_{\mathrm{e}}^{\mathrm{eff}}\lvert\nabla\varphi_{\mathrm{e}}\rvert^{2}+\sigma_{\mathrm{ion}}^{\mathrm{eff}}\lvert\nabla\varphi_{\mathrm{e}}\rvert^{2}+S_{1}h_{1}$ where T represents temperature (K) and ϕ is potential (V)
Component conservation equation	$\frac{\partial(\varepsilon c_i)}{\partial t}+\nabla\cdot(\varepsilon\vec{u}c_i)=\nabla\cdot(D_i^{\mathrm{eff}}\nabla c_i)+S_i$ where S_{i} is for $\mathrm{H_2}=-\frac{i_{\mathrm{anode}}}{2F}$ and $\mathrm{O_2}=\frac{i_{\mathrm{cathode}}}{4F}$, $\mathrm{H_2O}=\frac{i_{\mathrm{cathode}}}{2F}$ For ordered catalyst layers $D_{\mathrm{i}}^{\mathrm{eff}}=D_i\nu$ where $\nu=1-\nu_{\mathrm{s}}-\nu_{\mathrm{n}}-s$ and $\nu_{\mathrm{s}}=\left(\frac{1}{\rho_{\mathrm{Pt}}}+\frac{1-ml_{\mathrm{Pt}}}{ml_{\mathrm{Pt}}\rho_{\mathrm{c}}}\right)\frac{m_{\mathrm{Pt}}}{L}$ ν represents porosity, ν_{n} represents ionomer volume friction, ν_{s} represents the carbon volume fraction, and ml_{Pt} represents mass percentage of platinum or platinum loading
Charge conservation equation	Electron conservation electrons are driven by $\nabla\cdot(\sigma_{\mathrm{e}}^{\mathrm{eff}}\nabla\varphi_{\mathrm{e}})+S_{\mathrm{e}}=0$ Meanwhile proton conservation electrons are driven by $\nabla\cdot(\sigma_{\mathrm{ion}}^{\mathrm{eff}}\nabla\varphi_{\mathrm{ion}})+S_{\mathrm{ion}}=0$ where S_{e} and S_{ion} are the electron generation rates, for $-i_{\mathrm{anode}}$ and i_{cathode}
Liquid water transport equation	Transport of water that flows in a channel is driven by $\frac{\partial(\varepsilon\rho_1 s)}{\partial t}+\nabla\cdot(\rho_1\overrightarrow{u_1}s)=S_1$ where s is liquid water saturation and S_1 is the water vapor condensation rate The transport of liquid water can be driven by $\frac{\partial(\varepsilon\rho_1 s)}{\partial t}+\nabla\cdot\left(\rho_1\frac{{K_{\mathrm{s}}}^{3}}{\mu_1}\frac{\mathrm{d}p_{\mathrm{c}}}{\mathrm{d}s}\nabla s\right)=S_1$ The water vapor condensation rate if $P_{\mathrm{wv}} > P_{\mathrm{sat}}$ follows $S_1=k_{\mathrm{e}}(1-s)\frac{P_{\mathrm{wv}}-P_{\mathrm{sat}}}{RT}M_{\mathrm{H_2O}}$, and when $P_{\mathrm{wv}} < P_{\mathrm{sat}}$ it follows $S_1=k_{\mathrm{c}}s\frac{P_{\mathrm{wv}}-P_{\mathrm{sat}}}{RT}M_{\mathrm{H_2O}}$
Electrochemical reaction equation	The electrochemical reaction in catalyst layers follows the Butler–Volmer equation $i_{\mathrm{anode}}=(1-s)A_{\mathrm{anode}}i_{\mathrm{anode}}\left(\frac{C_{\mathrm{H_2}}}{C_{H_{2,\mathrm{reff}}}}\right)^{\gamma\ \mathrm{anode}}\exp\left(\frac{\alpha_{\mathrm{anode}}F}{RT}\eta_{\mathrm{anode}}\right)$ $i_{\mathrm{cathode}}=(1-s)A_{\mathrm{cathode}}i_{\mathrm{cathode}}\left(\frac{C_{\mathrm{O_2}}}{C_{\mathrm{O_{2,reff}}}}\right)^{\gamma\ \mathrm{cathode}}\exp\left(\frac{\alpha_{\mathrm{cathode}}F}{RT}\eta_{\mathrm{cathode}}\right)$ where A represents the specific active surface area; for OCLs the equation is as follows: $A=\frac{m_{\mathrm{Pt}}A^{0}}{L}$ A^{0} represents the surface area of the catalyst per mass and L is the thickness of the catalyst layer C represents the hydrogen or oxygen content and η represents the overpotential of the electrode For $\eta_{\mathrm{anode}}=\varphi_{\mathrm{e}}-\varphi_{\mathrm{ion}}$ and $\eta_{\mathrm{cathode}}=\varphi_{\mathrm{e}}-\varphi_{\mathrm{ion}}-E_0$, where E_0 represents open circuit voltage
Oxygen transport in OCLs	Diffusion in the pores follows the equation $\frac{\partial C_{\mathrm{O_2}}}{\partial t}=\nabla(D_{\mathrm{p}}\nabla C_{\mathrm{O_2}})$ where $C_{\mathrm{O_2}}$ represents the oxygen concentration and D_{p} is the diffusivity The oxygen content dissolved in the outermost layer of the water film $C_{\mathrm{O_2}}$ following Henry's law follows $C_{\mathrm{O_{2,w}}}=\frac{C_{\mathrm{O_2}}}{k_{\mathrm{h,O_2}}}$ where $C_{\mathrm{O_2}}$ represents oxygen content and $k_{\mathrm{h,O_2}}$ represents Henry's constant The oxygen concentration gradient caused by resistance of oxygen that passes through follows $D_{\mathrm{O_2}}\left(\frac{d^{2}C_{\mathrm{O_2}}}{dr^{2}}+\frac{d_{C_{\mathrm{O_2}}}}{dr}\frac{1}{r}\right)=0$

Table 3 Developed equations related to a local oxygen transport model[63]

Regions	Equations
Bulk pores to the water	$C_{\mathrm{O_2}1} = C_{\mathrm{O_2}g}\dfrac{RT}{H_{\mathrm{O_2,w}}}$ where $C_{\mathrm{O_2}}$ indicates the amount of oxygen that is produced as a result of the interfacial dissolution process and $H_{\mathrm{O_2,w}}$ is the Henry's constant for oxygen
The water film	$N_{\mathrm{O_2}} = (C_{\mathrm{O_2}2} - C_{\mathrm{O_2}1})\dfrac{D_{\mathrm{O_2,w}}}{\delta_{\mathrm{w}}}$ where $D_{\mathrm{O_2,w}}$ is the diffusion coefficient of oxygen in the water film and $C_{\mathrm{O_2},2}$ is the oxygen concentration resulting from oxygen diffusion in the thin water film. The thickness of the accumulated water film is represented by δ_{w}, while the oxygen flux related to local oxygen transport activities is indicated by $N_{\mathrm{O_2}}$ Faraday's law can be used to describe the oxygen flux in a local oxygen transport model $N_{\mathrm{O_2}} = \dfrac{j_{\mathrm{c}}}{4Fa_{\mathrm{ion}}}$ where an ion represents the volumetric surface area of the active site within the ionomer
Water to the ionomer	$C_{\mathrm{O_2,w-ion}} = C_{\mathrm{O_2}2}\dfrac{H_{\mathrm{O_2,\,ion}}}{H_{\mathrm{O_2,w}}};\ N_{\mathrm{O_2}} = (C_{\mathrm{O_2}3} - C_{\mathrm{O_2,w-ion}})k_{\mathrm{w-ion}};\ \dfrac{1}{k_{\mathrm{w-ion}}} = \dfrac{1}{3}\dfrac{\delta_{\mathrm{ion}}}{D_{\mathrm{O_2,ion}}}$ where $C_{\mathrm{O_2}3}$ and $C_{\mathrm{O_2,w-ion}}$ represent the oxygen concentrations arising from the dissolution and interfacial processes, $H_{\mathrm{O_2,ion}}$ and $H_{\mathrm{O_2,w}}$ represent Henry's constant of oxygen in the ionomer and water. $D_{\mathrm{O_2,ion}}$ represents the diffusion coefficient of oxygen within the ionomer, δ_{ion} denotes the thickness of the ionomer layer, and $k_{\mathrm{w-ion}}$ signifies the water–ionomer interfacial resistance.[112]
The ionomer film	$N_{\mathrm{O_2}} = (C_{\mathrm{O_2}4} - C_{\mathrm{O_2}3})\dfrac{D_{\mathrm{O_2,ion}}}{\delta_{\mathrm{ion}}}$ where $C_{\mathrm{O_2},4}$ represents the oxygen concentration that results from the ionomer film's oxygen diffusion mechanism
Ionomer to the Pt surface	$C_{\mathrm{O_2Pt}} = C_{\mathrm{O_2max}}\dfrac{K_{\mathrm{L}}C_{\mathrm{O_2,4}}}{1 + K_{\mathrm{L}}C_{\mathrm{O_2,4}}}C_{\mathrm{O_2max}} = \dfrac{\theta_{\mathrm{max}}}{N_{\mathrm{A}}}A_{\mathrm{Pt}}\rho_{\mathrm{O_2}}$ The Langmuir adsorption equation can be used to determine how much oxygen is adsorbed on the Pt surface in order to investigate interfacial resistances. In this equation, K_{L} is the Langmuir adsorption coefficient, θmax is the maximum oxygen adsorption coverage on the Pt surface, N_{A} is the Avogadro constant, and A_{Pt} is the electrochemical specific surface area of Pt
Oxygen transport resistance	The total oxygen transfer ratio (OTR) is the ratio of the oxygen concentration change to the oxygen flux of all transport systems $R_{\mathrm{total}} = \dfrac{C_{\mathrm{O_2CH}} - C_{\mathrm{O_2Pt}}}{N_{\mathrm{O_2}}} = \dfrac{4F(C_{\mathrm{O_2CH}} - C_{\mathrm{O_2Pt}})}{i}$ The oxygen content in channels is represented by $C_{\mathrm{O_2,CH}}$, the oxygen flux by $N_{\mathrm{O_2}}$, and the current density by i The logarithmic normalization technique is utilized for computing local OTRs in both limiting and non-limiting current scenarios, as the influence of the local oxygen concentration on volumetric current density is logarithmic $r_i = \log\left(\dfrac{C_{\mathrm{O_2,i}}}{C_{\mathrm{O_2,i+1}}}\right)$ The equation illustrates the relationship between the logarithmically normalized oxygen concentration (c_{i}) and logarithmically normalized oxygen transport resistance (r_{i}) The total logarithmic normalized OTR can be broken down into resistances caused by diffusive and interfacial processes. These include gas–water interfacial resistance ($r_{\mathrm{g-w,\,int}}$), water diffusive resistance ($r_{\mathrm{w,dif}}$), water–ionomer interfacial resistance ($r_{\mathrm{w-ion,\,int}}$), ionomer diffusive resistance ($r_{\mathrm{ion,dif}}$), and ionomer–Pt interfacial resistance ($r_{\mathrm{ion-Pt,int}}$). The five local transport processes may be directly compared and their impacts can be quantified using this method, which helps identify the stage in the local oxygen transport processes that determines the rate $r_{\mathrm{total,local}} = r_{\mathrm{g-w,int}} + r_{\mathrm{w,dif}} + r_{\mathrm{w-ion,int}} + r_{\mathrm{ion,dif}} + r_{\mathrm{ion-Pt,int}}$

modelling to explore potential designs to improve fuel cell performance that are widely open.

Future research should focus on developing multiscale computational models that combine atomic-level catalyst interactions with macroscopic transport phenomena. Current models often oversimplify the complexity of the interactions between mass transport, reaction kinetics, and water management in ordered catalyst layers (OCLs). Integration of artificial intelligence (AI) and machine learning can accelerate the optimization of OCL geometry, such as pore alignment and ionomer distribution, to reduce tortuosity and maximize platinum (Pt) utilization. However, model validation against experimental data, especially under dynamic operating conditions such as start-stop or load changes, remains a critical challenge for real-world fuel cell applications.

4.2. Advanced structures and scalability challenges

The type of layer structure has been investigated in order to identify key attributes such as mass transport, ohmic resistance, Pt use, water management, and durability. The figure illustrates the type of configuration of catalyst layers. The materials employed in these constructions may be homogeneous or heterogeneous. Some achievable and outstanding electrode structures that have been successfully applied or can be adapted in PEMFCs will be discussed below (Fig. 9).

The template-assisted electrodeposition approach has been used to effectively produce single-walled polypyrrole (PPy) nanotube arrays (NTAs) and multi-walled MnO_2/PPy/MnO_2 nanotube arrays (TNTAs).[113] The design consisted of single-walled PPy NTAs with outer diameters of around 500 nm and tunable interior diameters ranging from 200 to 400 nm. Wall thicknesses varied between 19 and 120 nm depending on the electropolymerization time. The triple-layered MnO_2/PPy/MnO_2 TNTAs, composed of inner MnO_2, middle PPy, and outside MnO_2 layers with thicknesses of 65 nm, 125 nm, and 60 nm, have an outer diameter of roughly 700 nm and a length of 2 μm. The PPy NTAs had a specific capacitance (C_{sp}) of ~350 F g^{-1} at a scan rate of 1 mV s^{-1}. However, the MnO_2/PPy/MnO_2 TNTAs had a higher C_{sp} of ~379 F g^{-1} at 5 mV s^{-1}, exceeding that of MnO_2 NTAs (~277 F g^{-1}). Furthermore, the MnO_2/PPy/MnO_2 TNTAs demonstrated superior rate capability, with only a 37% reduction in C_{sp} at high scan rates (5–250 mV s^{-1}), as opposed to a 64% reduction for MnO_2 NTAs. Long-term cycling stability experiments demonstrated that the MnO_2/PPy/MnO_2 TNTAs retained 92.2% of their original C_{sp} after 1000 cycles at 10 mV s^{-1}, surpassing both PPy NTAs (81.4%) and MnO_2 NTAs (47.2%). Furthermore, the MnO_2/PPy/MnO_2 TNTAs demonstrated impressive energy and power densities, delivering up to 68 W h kg^{-1} and 37.4 kW kg^{-1}, respectively, fulfilling the power requirements for hybrid vehicle applications. The study emphasizes the advantages of hollow, multi-walled designs with large surface areas and well-organized pore channels, which promote effective material utilization and electrochemical performance.

A coaxial nanowire electrode (CANE) was also developed with the main objective of addressing the drawbacks of conventional Pt/C electrodes, such as limited durability, rapid degradation, and poor mass transmission. In this study, conventional electrodes involving dispersed Pt nanoparticles supported on carbon with ionomer binders generate a random, tortuous structure, whereas the CANE has a vertically aligned nanowire array with ionomer cores encapsulated by nanoscale Pt sheets. The results show that after 5.000 support accelerated stress testing (AST) cycles, the CANE lost only 2% of its performance at 0.7 V, compared to 87% for conventional Pt/C. After 30 000 catalyst AST cycles, the CANE showed just a 5% performance loss, whereas Pt/C lost 27%. The CANE had a slight decrease in electrochemical surface area (ECSA) (8.3 m^2 g^{-1} to 8.5 m^2 g^{-1}), whereas Pt/C lost over 70% of its ECSA. The CANE retained 99% of its ECSA, whereas Pt/C retained only 46%. At 0.6 V, the CANE achieved a current density of 1.51 A cm^{-2} after support AST, compared to 0.23 A cm^{-2} with Pt/C. At 0.7 V, this structure maintained a current density of 0.79 A cm^{-2} after catalyst AST, as opposed to 0.67 A cm^{-2} for Pt/C.[114]

Orthogonally aligned nanofiber (OAN) layers were also compared to random nanofiber layers (RNLs) in the PEMFC[115] application. The results indicated that RNL structures outperformed OAN structures. RNLs carbonized at 900 °C had an in-plane conductivity of 6.7 S cm^{-1}, compared to 1.53 S cm^{-1} for OAN layers under similar conditions. OAN layer performance is limited by shorter electrical paths, delamination during processing, and thicker ionomer pockets that impede oxygen transfer. Despite these limitations, OAN layers performed comparably to RNLs under high-temperature, low-humidity conditions, most likely due to improved ionomer connection

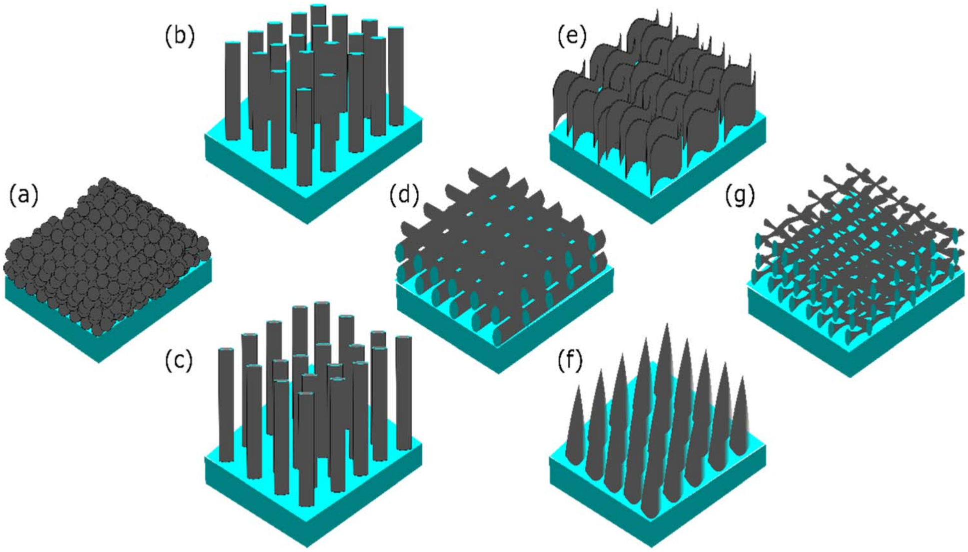

Fig. 9 Type of structure of electrodes, (a) bulk, (b) vertically aligned, (c) vertically aligned with tubes, (d) orthogonally aligned, (e) nanosheet/nanowall, (f) grooved and (g) nanoporous.

Table 4 Compilation of existing structures, fabrication methods and key performance

Author	Year	Catalyst structure	Fabrication method	Catalyst performance	Ref.
Debe *et al.*	2006	Nanostructured thin film (NSTF)	Organic film coating with a Pt/Pt-alloy without an ionomer	Pt loading: 0.15 mg$_{Pt}$ cm^{-2}, ~33% surface area loss in 9000 cycles, and activation energy 52 kJ per mole	118
Kim *et al.*	2013	Inverse-opal (IO) structure with 500 nm macropores	Electrodeposition onto a GDL	Pt loading: 0.12 mg cm^{-2}, ECSA: 24.13 m2 g^{-1}, Pt utilization: 60.27(%), current density: 1056 mA cm^{-2}, and maximum power density 836 mW cm^{-2}	55
Murata *et al.*	2014	Pt on vertically aligned CNTs (VACNTs)	Decal-transfer from the substrate to the membrane	Current density: 2.6 A cm^{-2} at 0.6 V and platinum (Pt) loading 0.1 mg cm^{-2}	118
Tian *et al.*	2011	Pt/VACNTs with vertically aligned CNTs	Plasma enhanced chemical vapor deposition (PECVD)	Ultra-low Pt loading down to 35 μg cm^{-2} was comparable to that of the commercial Pt catalyst, 400 μg cm^{-2}	94
Brodt *et al.*	2013	Nanofiber-based catalyst	Electrospinning	Power density: 470 mW cm^{-2} at 0.65 V and a Pt loading of 0.10 mg cm^{-3}	119
Wang *et al.*	2014	Nanoparticle/nanofiber electrodes	Electrospinning	Pt utilization: 0.024 g$_{Pt}$ kW^{-1} (42 kW g$_{Pt}$$^{-1}$) and Pt loading at 0.022 mg$_{Pt}$ cm^{-2}	120
Chen *et al.*	2014	Nanofiber 3D network	Electrospinning	PtRu loading within the NNCL: 1.0 mg cm^{-2} and power density 33.0 ± 19 mW cm^{-2}	121
Zhang *et al.*	2020	Hollow Pt–Pd nanocages	Pd-core removal	High CO_2 conversion and CO selectivity	122
Schuler *et al.*	2020	Porous transport layer materials with tailored interfaces	Cosintering	Thermal conductivities of ≈10 W mK^{-1} and a current density of 2 A cm^{-2}; multilayer materials show on average ≈60 mV lower mass transport overpotential	123
Yu *et al.*	2015	Reactive spray-deposited catalyst layer	Reactive spray deposition technology (RSDT)	2.45 mW μg$_{Pt,total}$$^{-1}$ in air and 4.8 mW μg$_{Pt,total}$$^{-1}$	124
Sun *et al.*	2019	Nafion-nanofiber-based	Electrospinning	Power density of 1.39 W cm^{-2} at 70 °C and 100% RH	125
Zheng *et al.*	2017	Nanostructured ultrathin catalyst layer based on open-walled PtCo bimetallic nanotube arrays	Magnetron sputtering and thermal annealing	Power density: 14.38 kW g$_{Pt}$$^{-1}$ and Pt loading of 52.7 μg cm^{-2}	126
Zhang *et al.*	2021	Core–shell nanoparticles	Co-reduction method	Mass activity reduced to 1.13 A mg$_{Pt}$$^{-1}$ for Pd@PtNi/C, 1.29 A mg$_{Pt}$$^{-1}$ for Pd@PtNiFe/C, and 1.6 A mg$_{Pt}$$^{-1}$ for Pd@PtNiCu/C	127
Wang *et al.*	2016	Pt-based icosahedral nanocages	Selective etching of Pd@Pt$_{4.5}$L	Activity of 3.50 mA cm^{-2}	128
Bu *et al.*	2016	Biaxially strained PtPb/Pt core/shell nanoplate	Alloying PtPb (110) facets	Mass activities of 7.8 milliamperes (mA) per centimeter squared and 4.3 amperes per milligram of platinum at 0.9 volts	129
Li *et al.*	2016	Ultrafine jagged platinum nanowires	Electrochemical dealloying (leaching)process	Mass activity of 13.6 amperes permilligram of Pt	130
Lu *et al.*	2016	3D PtPd nanodendrites	Modified wet chemical reduction	Power density: 0.73 W cm^{-2} at 0.6 V	131
Fidiani *et al.*	2022	Au-doped PtAg nanorod electrode	One-step wet chemical reduction method	Power density: ~0.61 W cm^{-2}	132

management under dry conditions. Optimization efforts determined that an ionomer-to-carbon ratio (I/C) of 0.158, with a film thickness of about 60 nm, was optimal for obtaining the optimum performance in both configurations. This design resulted in a fivefold increase in current density at 600 mV compared to traditional carbon black (V50) with 157 μg per cm^2 Pt loading. An excessive ionomer produced thick films that increased oxygen transport resistance, especially in high-potential regions, lowering performance. Further improvement of CNF designs is recommended to meet constraints in OAN structures. Improvements include fine-tuning fiber alignment operations to increase inter-fiber communication, minimizing delamination during fabrication, and optimizing ionomer deposition methods to avoid thick ionomer pockets from appearing. These solutions have the potential to maximize the performance of OAN structures while retaining RNL's exceptional features.

Another study reported successfully fabricating and investigating the structure of ultrathin mesoporous Co_3O_4 nanosheets grown on nickel foam *via* a simple hydrothermal method.[116] This design has an average thickness of around 10 nm with mesopores ranging from 2 to 10 nm. This nanosheet structure demonstrates exceptional electrochemical performance, with a specific capacitance of 2194 F g^{-1} at a current density of 1 A g^{-1} in 1 M KOH solution. Despite the high current density of 15 A g^{-1}, the specific capacitance remains at 1198 F g^{-1}, suggesting strong rate capability. Furthermore, the electrode retains 93.1% of its maximal capacitance after 5000 charge–discharge cycles, demonstrating outstanding cycling stability. The mesoporous shape improves ion transport and accessibility to electroactive sites, with a BET surface area of 102 $m^2\ g^{-1}$. Electrochemical impedance spectroscopy supports a low charge transfer resistance (R_{ct}) of 2.0 Ω, highlighting the effectiveness of the nanosheet structure. Compared to typical electrodes, Co_3O_4 nanosheets have higher energy and power densities, with energy densities of 76.1 $W\ h\ kg^{-1}$ at 0.25 $kW\ kg^{-1}$ and 41.6 $W\ h\ kg^{-1}$ at 3.8 $kW\ kg^{-1}$.

Grooved electrode design has been shown to improve the resilience and performance of PEMFCs. Conventional electrodes utilize a random mixture of carbon–platinum (Pt/C) catalysts and ionomers to form tortuous networks for ion and oxygen transport. In contrast, grooved electrodes have high-ionomer-content ridges to facilitate proton (H^+) transport and grooves to enhance oxygen (O_2) diffusion, creating distinct transport pathways. The grooved electrode outperforms state-of-the-art conventional electrodes by up to 50% under standard operating conditions.[117]

The inverse opal (IO) structure, a three-dimensional (3D) ordered microporous platinum (Pt) electrode, has also been shown to perform better in reduced Pt loading mass transfer owing to unique structural advantages. In this study, conventional MEA randomly distributed carbon-supported Pt particles with tortuous pathways for reactant diffusion are compared to an IO electrode, which has a periodic, interconnected microporous structure with low tortuosity fabricated *via* colloidal crystal templating and electrodeposition. This report stands out in its fabrication stage because it is inserted directly into the MEA without requiring an additional transfer step. Enhanced Mass Transfer: the IO electrode's open and interconnected pores allow for faster reactant and product diffusion, improving current density. The results reveal that at 0.6 V and in fully humid circumstances, the IO-based MEA achieves 440 $mA\ cm^{-2}$, compared to 235 $mA\ cm^{-2}$ for a conventional MEA. At ambient humidity, the IO-based MEA's current density decreases by 37% (from 790 to 495 $mA\ cm^{-2}$), while that of the conventional MEA decreases by 45% (from 666 to 367 $mA\ cm^{-2}$). The IO-based MEA achieves a maximum power density of 320 $mW\ cm^{-2}$ at 0.12 $mg_{Pt}\ cm^{-2}$, surpassing the standard MEA's 269 $mW\ cm^{-2}$ 54. Table 4 compiles the outline of the existing catalyst structures and the fabrication method. It also addresses the key performance parameters.

In terms of manufacturing, scalability remains a significant barrier for nanoordered catalyst layers. Existing methods such as spray deposition,[133] screen printing,[134] and roll-to-roll[135] processing limit the potential for converting laboratory-scale work to commercial production. However, it has been widely acknowledged that achieving nanoorder while maintaining performance necessitates refined catalyst ink compositions and deposition protocols.[136–139] In terms of versatility, the ordered catalyst layer is fairly fulfilled for instance considering that exploration of optimization methods such as Taguchi design, response surface methodology, and genetic algorithms has been embraced to be applied to the extent of optimization parameters of fabrication.[140,141]

Advanced characterisation methods, such as X-ray microscopy and electron tomography, are critical for understanding nanostructured catalyst layers and driving the development of scalable manufacturing procedures. These devices provide distinctive perspectives into the topological topologies of nanostructured CLs. Researchers can utilize these approaches to visualize ionomer distribution, catalyst placement, and pore structures on multiple length scales, allowing scientists to optimize CL design.

Regarding durability, strategies such as promoting corrosion-resistant supports, optimizing ionomer distribution, and manufacturing protective coatings for Pt nanoparticles demonstrate promise in improving CL stability.[142] Furthermore, recycling solutions for recovering precious metals from spent CLs are critical for reducing PEMFCs' environmental effect while increasing their economic viability.[143–146]

Scalability of manufacturing and cost-effectiveness of production are major obstacles in transforming laboratory-scale OCL designs—such as vertically aligned carbon nanotube (VACNT) structures or inverse opals—into commercial products. Techniques such as electrospinning and atomic layer deposition (ALD) promise high precision, but are still limited by cost and production speed. The development of roll-to-roll methods, 3D printing, or template-based approaches needs to be optimized to achieve efficient mass production. Innovations in catalyst ink formulation, including using non-platinum metal-based hybrid materials, could reduce the reliance on precious metals. The main challenge remains maintaining structural integrity and electrochemical performance during large-scale production processes.

Improving durability and water management remain crucial areas of focus. Although OCLs improve water drainage, the risk of flooding or dry-out under extreme conditions still exists. Adaptive materials with tunable hydrophobicity or hierarchical pore structures need to be developed to dynamically regulate water. Integration of materials such as graphene oxide or metal–organic frameworks (MOFs) into OCLs can optimize proton conductivity while preventing ionomer accumulation. Ultrathin protective layers, such as ceramics or oxidation-resistant polymers, may be a breakthrough to protect Pt nanoparticles from dissolution. However, the balance between mechanical stability and electrochemical activity in these hybrid systems still requires in-depth exploration. The fabrication methodologies for 3D ordered catalyst layers have been studied. Table 5 summarizes the approaches, which included atomic layer deposition, electrospinning, template-assisted porous stacking, supported-type electrodes, self-organizing structures, and 3D printing.

4.3. Trends and research outlook

Over the last two decades, academic research on the topic of ordered catalyst layers has grown dramatically, as indicated by the increasing number of publications. Fig. 10a indicates that the publishing count increased from fewer than 50 articles per

Table 5 Summarized methods to fabricate ordered catalyst layers including their advantages, limitations and opportunities for development

Method	Advantages	Limitations	Opportunities for development
Deposition-type thin film (ALD)	• Improves utilization efficiency of Pt[147]	• High costs associated with specific templates	• Develop low-cost templates
	• Able to form thin films of various materials[147,148]	• Still in the initial laboratory stage	• Optimize ALD parameters
Electrospun metal nanofiber assemblies	• Efficient porous 3D ordered CLs[149–151]	• Lower production rate	• Innovation for electrospinning machinery to enhance the output
	• Large surface area, high conductivity, and excellent structural stability[152]	• Challenges in fabricating nanofibers with sub-10 nm diameters	• Improve process control for diameter optimization
Template-assisted porous stacking	• Enables providing accurate manufacturing of 3D ordered CL architectures	• Complicated preparation	• Shorten and reorganise fabrication techniques
	• Improves the performance including mass transport, electrical conductivity, the number of active sites, reaction rate, and the stability of the electrode CL[55]	• Risk of structure collapse	• Optimize template removal processes to minimize structural damage
Ordered supporter-type electrodes	• Improve ECSA[153–158]	• High costs	• Cost-efficient materials as alternatives
	• Enhance the conductivity and surface area[159,160]	• Durability issues	• Optimize designs to enhance durability
1D nanostructure self-organizing networks	• Enhanced catalytic activity and flexibility in alloy composition, atomic ratio, and surface structure design[161–164]	• Low ECSA[165]	• Self-supporting 3D ordered CLs for new-generation electrodes
	• Less prone to dissolution and aggregation contributing to maintaining higher power density at low Pt loading[166–168]	• Limited catalyst loading[165] • Mechanical instability[165]	
3D printing patterns	• High resolution (<10 nm)[169–171] • High throughput[169–171] • Large-scale manufacturing[169–171] • Low cost[169–171]	• High costs due to the emerging stage of 3D printing technology	• Improvement in 3D printing methods to reduce costs

year in the early 2000s to 350 by 2023, indicating exponential development. This trend, which became more prominent after 2018, correlates with an increased emphasis on renewable energy sources and the use of advanced nanotechnology techniques. Such patterns reflect growing interest among academics worldwide, motivated by both the fundamental issues of catalysis and the practical applications of these layers.

Quantitatively, the annual publication rate increased by 15–20% between 2010 and 2018 and then climbed to over 30% after 2019. This expansion shows a shift towards multidisciplinary collaboration, which includes materials science, nanotechnology, and electrochemistry. For example, investigations on atomically exact design of catalyst layers utilizing techniques including atomic layer deposition (ALD) and computer modeling of catalytic systems have emerged.

Patents in Fig. 10b show how ordered catalyst layer technology is being used in real-world applications. Several major patent classifications highlight advancements in this field, including the use of nanotechnology for material design (B82Y30/00), precision deposition of catalytic layers (B01J37/02), and the use of platinum-group metals in electrocatalysis (H01M4/92). These patents address issues such as increased catalytic activity, lowered material prices, and improved structural stability. One major area of advancement is the creation of better production procedures for organized catalyst layers. Atomic layer deposition and molecular layer deposition allow for the controlled and uniform application of catalytic materials, which improves reaction kinetics by maximizing active site accessibility. For example, patents in the H01M4/92 category are concerned with platinum and platinum-alloy catalysts for oxygen reduction processes (ORR), which are crucial in fuel cells. Researchers are developing alternatives to platinum, such as cobalt or magnesium alloys, which can maintain performance while minimizing costs. Since 2015, the number of patents filed in this domain has steadily increased, in line with the growth in scholarly publications. Patent filings are concentrated in the United States, China, Japan, and Europe, indicating a strategic focus on clean energy technologies. Industry leaders such as Toyota, BASF, and Johnson Matthey, as well as research institutions, are pushing these advancements, displaying a collaborative effort to translate laboratory findings into commercial technologies.

A bibliometric analysis of ordered catalyst layer research indicates a strongly interconnected network of keywords that cover both fundamental and applied topics. Using tools such as the VOS viewer, these relationships can be grouped into two categories: foundational catalysis research and application-driven innovation.

As seen in Fig. 10c, the first cluster (red) concentrates on the fundamentals, with keywords such as "platinum", "nanoparticles", "carbon", "fuel cell", and "electrocatalysis". These words represent the primary problems of improving catalyst efficiency and durability while lowering prices. For example, the connection between "platinum" and "oxygen reduction reaction" demonstrates the importance of platinum-based catalysts in crucial energy conversion processes. This cluster's research frequently uses computational tools, such as density functional theory (DFT), to simulate and optimize atomic-scale catalyst behaviours.

The second cluster (green) focuses on applied research, with terms including "oxygen reduction reaction", "performance", "sintering", and "binary alloys". Catalyst layers are tailored to specific uses, including fuel cells, water splitting, and CO_2 reduction. The use of terms such as "cobalt alloys", "magnesium alloys", and "proton-exchange membranes" demonstrates continuous efforts to increase cost-effectiveness and sustainability by researching alternative materials and incorporating these catalysts into full energy systems. The links between

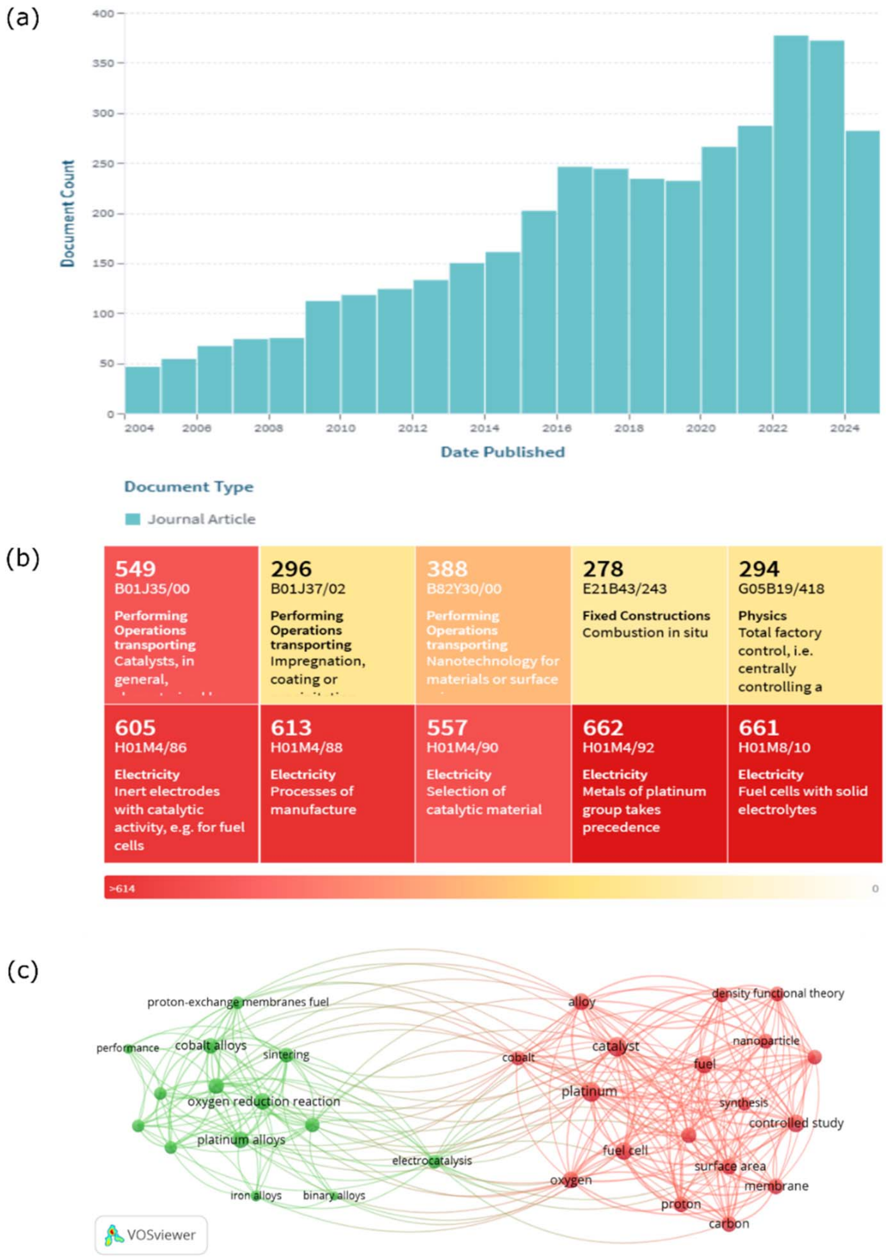

Fig. 10 (a) Trend of journal articles that have been published. (b) Top ten highest technologies that have been patented related to ordered catalyst layer fuel cells in two decades; data have been curated from lens.org accessed in November 2024. (c) Bibliometric analysis from the Scopus database that has been driven by VOSviewer software.

clusters demonstrate the interdisciplinary nature of this field. For example, "fuel cell" and "nanoparticles" act as bridge terminology between basic and applied research. This highlights the need for combining nanoscale design concepts with application-specific performance constraints. Furthermore, the increased use of terminology such as "energy resource" and "performance" indicates a broader trend toward sustainability and efficiency, which reflects global energy goals.

Integration of OCLs into full-scale PEMFC systems requires interdisciplinary collaboration between materials science, chemical engineering, and computer science. Validation of performance under real-world operating conditions—such as fluctuating humidity, high temperature, or variable pressure—should be performed through accelerated stress testing (AST) and *in situ* diagnostics. Materials with self-healing capabilities or responsiveness to external stimuli may provide a solution to long-term degradation. Remaining challenges include standardization of testing protocols, recycling of spent catalysts, and economic viability for sustainable commercialization. Synergy between academia, industry, and policymakers is needed to align technological innovation with global goals for the clean energy transition.

5. Conclusion

Proton Exchange Membrane Fuel Cells (PEMFCs) have advanced significantly over the last two centuries. The invention of catalyst layers has been a key achievement in permitting their growth and application. PEMFCs are one of the types with large potential for implementation, particularly in vehicles, and have advantages in terms of reducing CO_2 emissions. The development of PEMFCs also hinges on the method for advancing the catalyst due to platinum's expensive cost.

- Mass transport: as shown theoretically and experimentally, organized catalyst nanofibers can improve PEMFC performance by enhancing mass transport and applying Fick's law to describe gaseous diffusion in catalyst layers. The increase in oxygen diffusion in OCLs can also be ascribed to a reduction in Knudsen diffusion restrictions, since aligned holes in OCLs allow for more efficient molecular and Knudsen diffusion than in CCLs. In terms of tortuosity, the ordered arrangement of Pt particles decreases the requirement for tortuosity adjustments, making it easier for oxygen to diffuse. The effective diffusion coefficient in OCLs approaches the bulk value of oxygen diffusion, which is lower than that of CCLs.
- Reaction rate: efficient reactant access depends on the uniform distribution of Pt, which determines the availability of active sites for the reaction. In OCLs, Pt particles are uniformly distributed on aligned supports, maximizing Pt site exposure to reactive species. Furthermore, the overpotential increases because of the scarcity of Pt sites. This arrangement produces a higher exchange current density (i_0) and lower overpotentials.
- Pt utilization: the economic viability and value of proton exchange membrane fuel cells (PEMFCs) are heavily dependent on the efficiency with which platinum is used. In OCLs, Pt particles are arranged uniformly. This structure improves material movement efficiency, resulting in higher output power and reliability under ultra-low Pt loading.
- Water management: the ordered structure of OCLs can improve water management by creating specialized pathways for liquid water removal and reducing flooding.
- Power output: reduction of overpotential activation in the polarization curve of the OCL demonstrates greater performance in the polarization curve that is governed by the Butler–Volmer equation. The value of active surface area in OCLs is higher due to the more evenly distributed Pt. This raises the current density, resulting in a better polarization curve.

Future advancements to the ordered catalyst layer, such as modeling and simulation, could aid in understanding the phenomenon and providing new insights. The remaining problem in ordered catalysts is scalability-related production. Many structures have been designed to achieve the best possible structure. Development of this method is in turn increasing, demonstrating that interest in the issue remains high.

Data availability

The data supporting this article were manually retrieved from the following publicly available sources: Data for Fig. 10a and (b) were obtained from the lens.org database https://www.lens.org/ with keyword "ordered catalyst fuel cell" with filtering data published from 2004 to 2024, accessed in November 2024. Fig. 10c data were obtained from the Scopus database https://www.scopus.com/ and analysed using VOSviewer by the author. All data used in this article are publicly available from these databases and can be accessed by readers through these platforms.

Author contributions

Conceptualization, M. Y. and V. H.; writing – original draft, M. Y.; writing – review and editing, M. Y. and V. H.; visualization, M. Y.; supervision, V. H.; funding acquisition, V. H. All authors have read and agreed to the published version of the manuscript.

Conflicts of interest

There are no conflicts to declare.

Acknowledgements

The authors would like to express their gratitude to the Open Access Funding provided by the TU Graz Open Access Publishing Fund. Furthermore, the authors would like to acknowledge the IEA Research Cooperation on behalf of the Austrian Federal Ministry for Climate Action, Environment, Energy, Mobility, Innovation, and Technology and OeAD (Austria) for the Ernst Mach Grant ASEA-UNINET scholarship.

Notes and references

1 International Energy Agency (IEA), *World Energy Outlook*, 2023.

2 F. Schenuit, R. Colvin, M. Fridahl, B. McMullin, A. Reisinger, D. L. Sanchez, S. M. Smith, A. Torvanger, A. Wreford and O. Geden, Carbon Dioxide Removal Policy in the Making: Assessing Developments in 9 OECD Cases, *Front. clim.*, 2021, **3**, 1–22.

3 P. K. Pathak, A. K. Yadav and S. Padmanaban, Transition toward emission-free energy systems by 2050: Potential role of hydrogen, *Int. J. Hydrogen Energy*, 2023, **48**, 9921–9927.

4 R. E. Rosli, A. B. Sulong, W. R. W. Daud, M. A. Zulkifley, T. Husaini, M. I. Rosli, E. H. Majlan and M. A. Haque, A review of high-temperature proton exchange membrane fuel cell (HT-PEMFC) system, *Int. J. Hydrogen Energy*, 2017, **42**, 9293–9314.

5 U.S.DRIVE Fuel Cell Tech Team, DOE Technical Targets for Polymer Electrolyte Membrane Fuel Cell Components, **https://www.energy.gov/eere/fuelcells/doe-technical-targets-polymer-electrolyte-membrane-fuel-cell-components**.

6 Z. Huang, L. Su, Y. Yang, L. Gao, X. Liu, H. Huang, Y. Li and Y. Song, Three-Dimensional Simulation on the Effects of Different Parameters and Pt Loading on the Long-Term Performance of Proton Exchange Membrane Fuel Cells, *Sustainability*, 2023, **15**, 1–22.

7 A. Kongkanand and M. F. Mathias, The Priority and Challenge of High-Power Performance of Low-Platinum Proton-Exchange Membrane Fuel Cells, *J. Phys. Chem. Lett.*, 2016, **7**, 1127–1137.

8 M. N. Islam, A. B. Mansoor Basha, V. O. Kollath, A. P. Soleymani, J. Jankovic and K. Karan, Designing fuel cell catalyst support for superior catalytic activity and low mass-transport resistance, *Nat. Commun.*, 2022, **13**, 1–11.

9 J. Fan, M. Chen, Z. Zhao, Z. Zhang, S. Ye, S. Xu, H. Wang and H. Li, Bridging the gap between highly active oxygen reduction reaction catalysts and effective catalyst layers for proton exchange membrane fuel cells, *Nat. Energy*, 2021, **6**, 475–486.

10 C. M. Zalitis, D. Kramer and A. R. Kucernak, Electrocatalytic performance of fuel cell reactions at low catalyst loading and high mass transport, *Phys. Chem. Chem. Phys.*, 2013, **15**, 4329–4340.

11 K. Wang, T. Zhou, Z. Cao, Z. Yuan, H. He, M. Fan and Z. Jiang, Advanced 3D ordered electrodes for PEMFC applications: From structural features and fabrication methods to the controllable design of catalyst layers, *Green Energy Environ.*, 2024, **9**, 1336–1365.

12 S. Mo, L. Du, Z. Huang, J. Chen, Y. Zhou, P. Wu, L. Meng, N. Wang, L. Xing, M. Zhao, Y. Yang, J. Tang, Y. Zou and S. Ye, *Recent Advances on PEM Fuel Cells: from Key Materials to Membrane Electrode Assembly*, Springer Nature Singapore, 2023, vol. 6.

13 G. Yang, C. H. Lee, X. Qiao, S. K. Babu, U. Martinez and J. S. Spendelow, *Advanced Electrode Structures for Proton Exchange Membrane Fuel Cells: Current Status and Path Forward*, Springer Nature Singapore, 2024, vol. 7.

14 J. K. Koh, Y. Jeon, Y. Il Cho, J. H. Kim and Y. G. Shul, A facile preparation method of surface patterned polymer electrolyte membranes for fuel cell applications, *J. Mater. Chem. A*, 2014, **2**, 8652–8659.

15 X. Ren, Q. Lv, L. Liu, B. Liu, Y. Wang, A. Liu and G. Wu, Current progress of Pt and Pt-based electrocatalysts used for fuel cells, *Sustainable Energy Fuels*, 2019, **4**, 15–30.

16 J. Liu, S. Liu, F. Yan, Z. Wen, W. Chen, X. Liu, Q. Liu, J. Shang, R. Yu, D. Su and J. Shui, Ultrathin Nanotube Structure for Mass-Efficient and Durable Oxygen Reduction Reaction Catalysts in PEM Fuel Cells, *J. Am. Chem. Soc.*, 2022, **144**, 19106–19114.

17 M. Qi, Y. Zeng, M. Hou, Y. Gou, W. Song, H. Chen, G. Wu, Z. Jia, Y. Gao, H. Zhang and Z. Shao, Free-standing and ionomer-free 3D platinum nanotrough fiber network electrode for proton exchange membrane fuel cells, *Appl. Catal., B*, 2021, **298**, 120504.

18 H. Cho, S. Moon Kim, Y. Sik Kang, J. Kim, S. Jang, M. Kim, H. Park, J. Won Bang, S. Seo, K. Y. Suh, Y. E. Sung and M. Choi, Multiplex lithography for multilevel multiscale architectures and its application to polymer electrolyte membrane fuel cell, *Nat. Commun.*, 2015, **6**, 1–8.

19 S. Jang, M. Kim, Y. S. Kang, Y. W. Choi, S. M. Kim, Y. E. Sung and M. Choi, Facile Multiscale Patterning by Creep-Assisted Sequential Imprinting and Fuel Cell Application, *ACS Appl. Mater. Interfaces*, 2016, **8**, 11459–11465.

20 N. A. A. Qasem and G. A. Q. Abdulrahman, *A Recent Comprehensive Review of Fuel Cells: History, Types, and Applications*, 2024, vol. 2024.

21 C. Spiegel, *Designing and Building Fuel Cells*, 2007.

22 M. L. Perry and T. F. Fuller, A Historical Perspective of Fuel Cell Technology in the 20th Century, *J. Electrochem. Soc.*, 2002, **149**, S59.

23 B. C. H. Steele and A. Heinzel, Materials for fuel-cell technologies, *Nature*, 2001, **414**, 345–352.

24 O. Z. Sharaf and M. F. Orhan, An overview of fuel cell technology: Fundamentals and applications, *Renewable Sustainable Energy Rev.*, 2014, **32**, 810–853.

25 K. V. Kordesch, 25 Years of Fuel Cell Development (1951–1976), *J. Electrochem. Soc.*, 1978, **125**, 77C–88C.

26 A. S. Abdulkareem, A. S. Afolabi, N. Fungura, T. Mokrani and C. Mateescu, The Realities and Economic Benefit of the Utilization of Fuel Cells as an Alternative Source of Energy: A Review, *Energy Sources, Part B*, 2015, **10**, 404–411.

27 N. Alonso-Vante, Parameters Affecting the Fuel Cell Reactions on Platinum Bimetallic Nanostructures, *Electrochem. Energy Rev.*, 2023, **6**, 1–24.

28 G. Athanasaki, A. Jayakumar and A. M. Kannan, Gas diffusion layers for PEM fuel cells: Materials, properties and manufacturing – A review, *Int. J. Hydrogen Energy*, 2023, **48**, 2294–2313.

29 A. G. Olabi, T. Wilberforce and M. A. Abdelkareem, Fuel cell application in the automotive industry and future perspective, *Energy*, 2021, **214**, 118955.

30 G. Prieto, H. Tüysüz, N. Duyckaerts, J. Knossalla, G. H. Wang and F. Schüth, Hollow Nano- and Microstructures as Catalysts, *Chem. Rev.*, 2016, **116**, 14056–14119.

31 L. Qu, Z. Wang, X. Guo, W. Song, F. Xie, L. He, Z. Shao and B. Yi, Effect of electrode Pt-loading and cathode flow-field plate type on the degradation of PEMFC, *J. Energy Chem.*, 2019, **35**, 95–103.

32 Q. Wang, Z. Zhou, Y. Lai, Y. You, J. Liu, X. Wu, E. Terefe, C. Chen, L. Song, M. Rauf, N. Tian and S. Sun, Phenylenediamine-Based FeN, *J. Am. Chem. Soc.*, 2014, 10882–10885.

33 K. Liu, Z. Qiao, S. Hwang, Z. Liu, H. Zhang, D. Su, H. Xu, G. Wu and G. Wang, Mn- and N- doped carbon as promising catalysts for oxygen reduction reaction: Theoretical prediction and experimental validation, *Appl. Catal., B*, 2019, **243**, 195–203.

34 A. Fick, Ueber Diffusion, *Ann. Phys.*, 1855, **170**, 59–86.

35 Y. Wang and S. Wang, Evaluation and modeling of PEM fuel cells with the Bruggeman correlation under various tortuosity factors, *Int. J. Heat Mass Transfer*, 2017, **105**, 18–23.

36 D. A. G. Bruggeman, Berechnung verschiedener physikalischer Konstanten von heterogenen Substanzen. I. Dielektrizitätskonstanten und Leitfähigkeiten der Mischkörper aus isotropen Substanzen, *Ann. Phys.*, 1935, **416**, 636–664.

37 J. H. Nam and M. Kaviany, Effective diffusivity and water-saturation distribution in single- and two-layer PEMFC diffusion medium, *Int. J. Heat Mass Transfer*, 2003, **46**, 4595–4611.

38 P. A. García-Salaberri, A Numerical Assessment of Mitigation Strategies to Reduce Local Oxygen and Proton Transport Resistances in Polymer Electrolyte Fuel Cells, *Materials*, 2023, **16**, 1–19.

39 J. S. Yi and T. V. Nguyen, Erratum: "Multicomponent Transport in Porous Electrodes of Proton Exchange Membrane Fuel Cells Using the Interdigitated Gas Distributor", *J. Electrochem. Soc.*, 1999, **146**, 2000.

40 T. F. Cao, H. Lin, L. Chen, Y. L. He and W. Q. Tao, Numerical investigation of the coupled water and thermal management in PEM fuel cell, *Appl. Energy*, 2013, **112**, 1115–1125.

41 N. Zamel, N. G. C. Astrath, X. Li, J. Shen, J. Zhou, F. B. G. Astrath, H. Wang and Z. S. Liu, Experimental measurements of effective diffusion coefficient of oxygen-nitrogen mixture in PEM fuel cell diffusion media, *Chem. Eng. Sci.*, 2010, **65**, 931–937.

42 Y. Wang and S. Wang, Evaluation and modeling of PEM fuel cells with the Bruggeman correlation under various tortuosity factors, *Int. J. Heat Mass Transfer*, 2017, **105**, 18–23.

43 O. J. Curnick, B. G. Pollet and P. M. Mendes, Nafion®-stabilised Pt/C electrocatalysts with efficient catalyst layer ionomer distribution for proton exchange membrane fuel cells, *RSC Adv.*, 2012, **2**, 8368–8374.

44 Z. Zhan, H. Song, X. Yang, P. Jiang, R. Chen, H. B. Harandi, H. Zhang and M. Pan, Microstructure Reconstruction and Multiphysics Dynamic Distribution Simulation of the Catalyst Layer in PEMFC, *Membranes*, 2022, **12**, 1–16.

45 Q. Qi and W. Zhu, The three-zone composite productivity model for a multi-fractured horizontal shale gas well, *IOP Conf. Ser. Earth Environ. Sci.*, 2018, **121**, 052051.

46 K. J. Lange, P.-C. Sui and N. Djilali, Pore Scale Simulation of Transport and Electrochemical Reactions in Reconstructed PEMFC Catalyst Layers, *J. Electrochem. Soc.*, 2010, **157**, B1434.

47 K. Malek and M. O. Coppens, Knudsen self- and Fickian diffusion in rough nanoporous media, *J. Chem. Phys.*, 2003, **119**, 2801–2811.

48 M. A. Khan, B. Sundén and J. Yuan, Analysis of multi-phase transport phenomena with catalyst reactions in polymer electrolyte membrane fuel cells - A review, *J. Power Sources*, 2011, **196**, 7899–7916.

49 I. V. Zenyuk, P. K. Das and A. Z. Weber, Understanding Impacts of Catalyst-Layer Thickness on Fuel-Cell Performance *via* Mathematical Modeling, *J. Electrochem. Soc.*, 2016, **163**, F691–F703.

50 D. Mu, Z. S. Liu, C. Huang and N. Djilali, Determination of the effective diffusion coefficient in porous media including Knudsen effects, *Microfluid. Nanofluid.*, 2008, **4**, 257–260.

51 S. Whitaker, *Theory and Applications of Transport in Porous Media*, 2000, vol. 418.

52 W. G. Pollard and R. D. Present, On gaseous self-diffusion in long capillary tubes, *Phys. Rev.*, 1948, **73**, 762–774.

53 W. Li, X. Wang, Z. Chen, M. Waje and Y. Yan, Carbon nanotube film by filtration as cathode catalyst support for proton-exchange membrane fuel cell, *Langmuir*, 2005, **21**, 9386–9389.

54 M. M. Waje, W. Li, Z. Chen and Y. Yan, Effect of Catalyst Support Morphology on the PEMFC Performance, *ECS Meeting Abstr.*, 2006, **MA2006-02**, 550.

55 O. H. Kim, Y. H. Cho, S. H. Kang, H. Y. Park, M. Kim, J. W. Lim, D. Y. Chung, M. J. Lee, H. Choe and Y. E. Sung, Ordered macroporous platinum electrode and enhanced mass transfer in fuel cells using inverse opal structure, *Nat. Commun.*, 2013, **4**, 1–9.

56 C. Pacheco, R. Barbosa, A. Navarro-Montejo and L. C. Ordoñez, Theoretical analysis of the effect of isotropy on the effective diffusion coefficient in the porous and agglomerated phase of the electrodes of a PEMFC, *Sci. Rep.*, 2024, **14**, 1–12.

57 J. Gao, H. Wang, Z. Zhang, Y. Chen, D. Li, M. Zhou, M. Chai and Y. Li, Semi-ordered catalyst layer with ultra-low Pt loading for proton exchange membrane fuel cells, *J. Power Sources*, 2024, **606**, 234516.

58 Y. J. Wang, N. Zhao, B. Fang, H. Li, X. T. Bi and H. Wang, Carbon-Supported Pt-Based Alloy Electrocatalysts for the Oxygen Reduction Reaction in Polymer Electrolyte Membrane Fuel Cells: Particle Size, Shape, and

Composition Manipulation and Their Impact to Activity, *Chem. Rev.*, 2015, **115**, 3433–3467.

59 T. Maoka, Electrochemical reduction of oxygen on small platinum particles supported on carbon in concentrated phosphoric acid-II. Effects of teflon content in the catalyst layer and baking temperature of the electrode, *Electrochim. Acta*, 1988, **33**, 379–383.

60 J. Willsau and J. Heitbaum, The influence of Pt-activation on the corrosion of carbon in gas diffusion electrodes-A dems study, *J. Electroanal. Chem.*, 1984, **161**, 93–101.

61 J. O. Bockris and A. K. N. Reddy, *Modern Electrochemistry*, Kluwer Academic Publishers, 2nd edn, 2004, vol. 11.

62 N. P. Subramanian, T. A. Greszler, J. Zhang, W. Gu and R. Makharia, Pt-Oxide Coverage-Dependent Oxygen Reduction Reaction (ORR) Kinetics, *J. Electrochem. Soc.*, 2012, **159**, B531–B540.

63 P. Z. Lin, J. Sun, M. C. Wu and T. S. Zhao, A multiscale model for proton exchange membrane fuel cells with order-structured catalyst layers, *Int. J. Heat Mass Transfer*, 2022, **195**, 123092.

64 S. Anantharaj and S. Noda, How properly are we interpreting the Tafel lines in energy conversion electrocatalysis?, *Mater. Today Energy*, 2022, **29**, 101123.

65 O. van der Heijden, S. Park, R. E. Vos, J. J. J. Eggebeen and M. T. M. Koper, Tafel Slope Plot as a Tool to Analyze Electrocatalytic Reactions, *ACS Energy Lett.*, 2024, **9**, 1871–1879.

66 O. A. Petrii, R. R. Nazmutdinov, M. D. Bronshtein and G. A. Tsirlina, Life of the Tafel equation: Current understanding and prospects for the second century, *Electrochim. Acta*, 2007, **52**, 3493–3504.

67 C. Y. Du, T. Yang, P. F. Shi, G. P. Yin and X. Q. Cheng, Performance analysis of the ordered and the conventional catalyst layers in proton exchange membrane fuel cells, *Electrochim. Acta*, 2006, **51**, 4934–4941.

68 M. M. Hussain, D. Song, Z. S. Liu and Z. Xie, Modeling an ordered nanostructured cathode catalyst layer for proton exchange membrane fuel cells, *J. Power Sources*, 2011, **196**, 4533–4544.

69 M. Ye, L. Rong, X. Ma and W. Yang, Numerical Optimization of Triple-Phase Components in Order-Structured Cathode Catalyst Layer of a Proton Exchange Membrane Fuel Cell, *Energies*, 2023, **16**, 1–19.

70 K. Kodama, T. Nagai, A. Kuwaki, R. Jinnouchi and Y. Morimoto, Challenges in applying highly active Pt-based nanostructured catalysts for oxygen reduction reactions to fuel cell vehicles, *Nat. Nanotechnol.*, 2021, **16**, 140–147.

71 Z. Xia, Q. Wang, M. Eikerlitig and Z. Liu, Efffectiveness factor of Pt utilization in cathode catalyst layer of polymer electrolyte fuel cells, *Can. J. Chem.*, 2008, **86**, 657–667.

72 V. P. Zhdanov and B. Kasemo, Kinetics of rapid reactions on nanometer catalyst particles, *Phys. Rev. B:Condens. Matter Mater. Phys.*, 1997, **55**, 4105–4108.

73 E. Moguchikh, K. Paperj, A. Pavlets, A. Alekseenko, M. Danilenko and A. Nikulin, Influence of Composition and Structure of Pt-Based Electrocatalysts on Their Durability in Different Conditions of Stress-Test, *Advanced Materials*, ed. I. A. Parinov, S.-H. Chang and B. T. Long, Springer International Publishing, Cham, 2020, pp. 3–20.

74 M. Ko, E. Padgett, V. Yarlagadda, A. Kongkanand and D. A. Muller, Revealing the Nanostructure of Mesoporous Fuel Cell Catalyst Supports for Durable, High-Power Performance, *J. Electrochem. Soc.*, 2021, **168**, 024512.

75 C. Y. Ahn, J. E. Park, S. Kim, O. H. Kim, W. Hwang, M. Her, S. Y. Kang, S. Park, O. J. Kwon, H. S. Park, Y. H. Cho and Y. E. Sung, Differences in the Electrochemical Performance of Pt-Based Catalysts Used for Polymer Electrolyte Membrane Fuel Cells in Liquid Half-and Full-Cells, *Chem. Rev.*, 2021, **121**, 15075–15140.

76 D. S. Hwang, C. H. Park, S. C. Yi and Y. M. Lee, Optimal catalyst layer structure of polymer electrolyte membrane fuel cell, *Int. J. Hydrogen Energy*, 2011, **36**, 9876–9885.

77 S. Martin, P. L. Garcia-Ybarra and J. L. Castillo, High platinum utilization in ultra-low Pt loaded PEM fuel cell cathodes prepared by electrospraying, *Int. J. Hydrogen Energy*, 2010, **35**, 10446–10451.

78 M. Brodt, R. Wycisk and P. N. Pintauro, Nanofiber Electrodes with Low Platinum Loading for High Power Hydrogen/Air PEM Fuel Cells, *J. Electrochem. Soc.*, 2013, **160**, F744–F749.

79 M. Brodt, T. Han, N. Dale, E. Niangar, R. Wycisk and P. Pintauro, Fabrication, In-Situ Performance, and Durability of Nanofiber Fuel Cell Electrodes, *J. Electrochem. Soc.*, 2015, **162**, F84–F91.

80 X. Wang, F. W. Richey, K. H. Wujcik, R. Ventura, K. Mattson and Y. A. Elabd, Effect of polytetrafluoroethylene on ultra-low platinum loaded electrospun/electrosprayed electrodes in proton exchange membrane fuel cells, *Electrochim. Acta*, 2014, **139**, 217–224.

81 J. Stumper, M. Löhr and S. Hamada, Diagnostic tools for liquid water in PEM fuel cells, *J. Power Sources*, 2005, **143**, 150–157.

82 H. Li, Y. Tang, Z. Wang, Z. Shi, S. Wu, D. Song, J. Zhang, K. Fatih, J. Zhang, H. Wang, Z. Liu, R. Abouatallah and A. Mazza, A review of water flooding issues in the proton exchange membrane fuel cell, *J. Power Sources*, 2008, **178**, 103–117.

83 Z. X. P. K. Das, X. Li and Z. Liu, Effects of catalyst layer structure and wettability on liquid water transport in polymer electrolyte membrane fuel cell, *Int. J. Energy Res.*, 2011, **35**, 1325–1339.

84 J. J. Baschuk and X. Li, Modelling of polymer electrolyte membrane fuel cells with variable degrees of water flooding, *J. Power Sources*, 2000, **86**, 181–196.

85 C. Feng, Y. Li, K. Song and P. F. He, Structural characteristics, diffusion mechanism and mechanical behaviour of cathode catalyst layer, *Comput. Mater. Sci.*, 2020, **177**, 109572.

86 L. Liang, Y. Wei, X. Zhang, S. Chen, F. Yu, Z. Q. Tian and P. K. Shen, 3D Model of an Order-Structured Cathode Catalyst Layer with Vertically Aligned Carbon Nanotubes for PEM Fuel Cells under the Water Flooding Condition, *ACS Sustain. Chem. Eng.*, 2020, **8**, 695–705.

87 F. Gloaguen and R. Durand, Simulations of PEFC cathodes: An effectiveness factor approach, *J. Appl. Electrochem.*, 1997, **27**, 1029–1035.

88 A. Ohma, T. Mashio, K. Sato, H. Iden, Y. Ono, K. Sakai, K. Akizuki, S. Takaichi and K. Shinohara, Analysis of proton exchange membrane fuel cell catalyst layers for reduction of platinum loading at Nissan, *Electrochim. Acta*, 2011, **56**, 10832–10841.

89 A. Z. Weber, R. L. Borup, R. M. Darling, P. K. Das, T. J. Dursch, W. Gu, D. Harvey, A. Kusoglu, S. Litster, M. M. Mench, R. Mukundan, J. P. Owejan, J. G. Pharoah, M. Secanell and I. V. Zenyuk, A Critical Review of Modeling Transport Phenomena in Polymer-Electrolyte Fuel Cells, *J. Electrochem. Soc.*, 2014, **161**, F1254–F1299.

90 R. Vetter and J. O. Schumacher, Free open reference implementation of a two-phase PEM fuel cell model, *Comput. Phys. Commun.*, 2019, **234**, 223–234.

91 R. Vetter and J. O. Schumacher, Experimental parameter uncertainty in proton exchange membrane fuel cell modeling. Part I: Scatter in material parameterization, *J. Power Sources*, 2019, **438**, 227018.

92 A. Husar, S. Strahl and J. Riera, Experimental characterization methodology for the identification of voltage losses of PEMFC: Applied to an open cathode stack, *Int. J. Hydrogen Energy*, 2012, **37**, 7309–7315.

93 P. K. Bhattacharya, *Water Flooding in the Proton Exchange Membrane Fuel Cell*, Sp. Sci. Technol. IIT Kanpur Publ., 2015, vol. 15, p. 26.

94 Z. Q. Tian, S. H. Lim, C. K. Poh, Z. Tang, Z. Xia, Z. Luo, P. K. Shen, D. Chua, Y. P. Feng, Z. Shen and J. Lin, A highly order-structured membrane electrode assembly with vertically aligned carbon nanotubes for ultra-low Pt loading PEM fuel cells, *Adv. Energy Mater.*, 2011, **1**, 1205–1214.

95 M. Tan, W. Zhang, H. Liu, J. Zhang, Z. Guo, Q. Ma, Q. Xu, K. Hooshyari and H. Su, Revolutionizing high-temperature polymer electrolyte membrane fuel cells: Unleashing superior performance with vertically aligned TiO2 nanorods supporting ordered catalyst layer featuring Pt nanowires, *Fuel*, 2024, **357**, 130084.

96 L. Xuan, Y. Wang, J. Lan, K. Tao, C. Zhou and D. Mei, Development of cathode ordered membrane electrode assembly based on TiO2 nanowire array and ultrasonic spraying, *Energy*, 2023, **264**, 126243.

97 S. Murata, M. Imanishi, S. Hasegawa and R. Namba, Vertically aligned carbon nanotube electrodes for high current density operating proton exchange membrane fuel cells, *J. Power Sources*, 2014, **253**, 90–97.

98 M. Boni, C. S. Manikanta and V. Velisala, Experimental evaluation of proton exchange membrane fuel cell performance with sinusoidal flow channel designs, *Int. J. Hydrogen Energy*, 2024, **53**, 1233–1241.

99 M. Boni, V. Velisala, M. A. Kumar, K. Balu and A. Gundalabhagavan, Experimental evaluation of divergent parallel flow field effect on the proton exchange membrane fuel cell performance, *Ionics*, 2025, **31**, 2657–2670.

100 V. Velisala, G. Pullagura, N. Yarramsetty, S. Vadapalli, M. K. Boni and K. K. Gorantla, Three-Dimensional CFD Modeling of Serpentine Flow Field Configurations for PEM Fuel Cell Performance, *Arabian J. Sci. Eng.*, 2021, **46**, 11687–11700.

101 A. Al-Falahat and S. S. Alrwashdeh, Comprehensive engineering analysis of PEMFC gas diffusion layers: simulation-based evaluation of four groundbreaking structural modifications, *Results Eng.*, 2025, **25**, 104298.

102 D. M. Fadzillah, M. I. Rosli, M. Z. M. Talib, S. K. Kamarudin and W. R. W. Daud, Review on microstructure modelling of a gas diffusion layer for proton exchange membrane fuel cells, *Renewable Sustainable Energy Rev.*, 2017, **77**, 1001–1009.

103 A. Martín-Alcántara, L. González-Morán, J. Pino, J. Guerra and A. Iranzo, Effect of the Gas Diffusion Layer Design on the Water Management and Cell Performance of a PEM Fuel Cell, *Processes*, 2022, **10**, 1–16.

104 F. Vandenberghe, Towards a better understanding and modeling of catalyst and catalyst layer operation in Proton Exchange Membrane Fuel Cell, PhD thesis, Université Grenoble Alpes, 2023.

105 K. Park, Y. Wei, M. So, T. H. Noh, N. Kimura, Y. Tsuge and G. Inoue, Numerical analysis on influence of surface structures of cathode catalyst layers on performance of polymer electrolyte fuel cells, *Electrochem. Sci. Adv.*, 2023, **3**, 1–9.

106 P. C. Sui, X. Zhu and N. Djilali, *Modeling of PEM Fuel Cell Catalyst Layers: Status and Outlook*, Springer Singapore, 2019, vol. 2.

107 I. Terada and H. Nakagawa, Polymer Electrolyte Fuel Cell, *Kobunshi*, 2008, **57**, 498–501.

108 E. J. F. Dickinson and G. Smith, Modelling the proton-conductive membrane in practical polymer electrolyte membrane fuel cell (Pemfc) simulation: A review, *Membranes*, 2020, **10**, 1–53.

109 A. Z. Weber and J. Newman, Transport in Polymer-Electrolyte Membranes, *J. Electrochem. Soc.*, 2004, **151**, A311.

110 P. He, Y. T. Mu, J. W. Park and W. Q. Tao, Modeling of the effects of cathode catalyst layer design parameters on performance of polymer electrolyte membrane fuel cell, *Appl. Energy*, 2020, **277**, 115555.

111 S. M. Rao and Y. Xing, Simulation of nanostructured electrodes for polymer electrolyte membrane fuel cells, *J. Power Sources*, 2008, **185**, 1094–1100.

112 Q. Zhao, P. Majsztrik and J. Benziger, Diffusion and interfacial transport of water in Nafion, *J. Phys. Chem. B*, 2011, **115**, 2717–2727.

113 Z. L. Wang, R. Guo, L. X. Ding, Y. X. Tong and G. R. Li, Controllable template-assisted electrodeposition of single- and multi-walled nanotube arrays for electrochemical energy storage, *Sci. Rep.*, 2013, **3**, 1–8.

114 G. Yang, S. Komini Babu, W. P. R. Liyanage, U. Martinez, D. Routkevitch, R. Mukundan, R. L. Borup, D. A. Cullen and J. S. Spendelow, Coaxial Nanowire Electrodes Enable Exceptional Fuel Cell Durability, *Adv. Mater.*, 2023, **35**, 1–9.

115 S. Chan, J. Jankovic, D. Susac, M. S. Saha, M. Tam, H. Yang and F. Ko, Electrospun carbon nanofiber catalyst layers for polymer electrolyte membrane fuel cells: Structure and performance, *J. Power Sources*, 2018, **392**, 239–250.

116 D. Takimoto, S. Toma, Y. Suda, T. Shirokura, Y. Tokura, K. Fukuda, M. Matsumoto, H. Imai and W. Sugimoto, Platinum nanosheets synthesized *via* topotactic reduction of single-layer platinum oxide nanosheets for electrocatalysis, *Nat. Commun.*, 2023, **14**, 1–9.

117 C. H. Lee, W. J. M. Kort-Kamp, H. Yu, D. A. Cullen, B. M. Patterson, T. A. Arman, S. Komini Babu, R. Mukundan, R. L. Borup and J. S. Spendelow, Grooved electrodes for high-power-density fuel cells, *Nat. Energy*, 2023, **8**, 685–694.

118 M. K. Debe, Nanostructured Thin Film Electrocatalysts for PEM Fuel Cells - A Tutorial on Fundamental Characteristics and Practical Properties, *ECS Meeting Abstr.*, 2012, **MA2012-01**, 557.

119 M. Brodt, R. Wycisk, P. N. Pintauro, T. Han, N. Dale and K. Adjemian, Nanofiber Fuel Cell Electrodes I. Fabrication and Performance With Commercial Pt/C Catalysts, *ECS Meeting Abstr.*, 2013, **MA2013-02**, 1305.

120 X. Wang, F. W. Richey, K. H. Wujcik and Y. A. Elabd, Ultra-low platinum loadings in polymer electrolyte membrane fuel cell electrodes fabricated *via* simultaneous electrospinning/electrospraying method, *J. Power Sources*, 2014, **264**, 42–48.

121 P. Chen, H. Wu, T. Yuan, Z. Zou, H. Zhang, J. Zheng and H. Yang, Electronspun nanofiber network anode for a passive direct methanol fuel cell, *J. Power Sources*, 2014, **255**, 70–75.

122 H. Zhang, H. Xu, Y. Li and Y. Su, Octahedral core–shell bimetallic catalysts M@UIO-67 (M = Pt–Pd nanoparticles, Pt–Pd nanocages): Metallic nanocages that enhanced CO2 conversion, *Appl. Mater. Today*, 2020, **19**, 100609.

123 T. Schuler, J. M. Ciccone, B. Krentscher, F. Marone, C. Peter, T. J. Schmidt and F. N. Büchi, Hierarchically Structured Porous Transport Layers for Polymer Electrolyte Water Electrolysis, *Adv. Energy Mater.*, 2020, **10**, 1–12.

124 H. Yu, A. Baricci, R. Justin, Y. Wang, A. Casalegno, W. Mustain and R. Marica, Ultra-low Pt Loading Catalyst Layers for PEMFC Using Reactive Spray Deposition Technology, *ECS Trans.*, 2015, **69**, 487–496.

125 Y. Sun, L. Cui, J. Gong, J. Zhang, Y. Xiang and S. Lu, Design of a Catalytic Layer with Hierarchical Proton Transport Structure: The Role of Nafion Nanofiber, *ACS Sustain. Chem. Eng.*, 2019, **7**, 2955–2963.

126 Y. Zeng, Z. Shao, H. Zhang, Z. Wang, S. Hong, H. Yu and B. Yi, Nanostructured ultrathin catalyst layer based on open-walled PtCo bimetallic nanotube arrays for proton exchange membrane fuel cells, *Nano Energy*, 2017, **34**, 344–355.

127 Y. Zhang, K. Ye, Q. Gu, Q. Jiang, J. Qin, D. Leng, Q. Liu, B. Yang and F. Yin, Optimized oxygen reduction activity by tuning shell component in Pd@Pt-based core-shell electrocatalysts, *J. Colloid Interface Sci.*, 2021, **604**, 301–309.

128 X. Wang, L. Figueroa-Cosme, X. Yang, M. Luo, J. Liu, Z. Xie and Y. Xia, Pt-Based Icosahedral Nanocages: Using a Combination of {111} Facets, Twin Defects, and Ultrathin Walls to Greatly Enhance Their Activity toward Oxygen Reduction, *Nano Lett.*, 2016, **16**, 1467–1471.

129 L. Bu, N. Zhang, S. Guo, X. Zhang, J. Li, J. Yao, T. Wu, G. Lu, J. Y. Ma, D. Su and X. Huang, Biaxially strained PtPb/Pt core/shell nanoplate boosts oxygen reduction catalysis, *Science*, 2016, **354**, 1410–1414.

130 M. Li, Z. Zhao, T. Cheng, A. Fortunelli, C. Y. Chen, R. Yu, Q. Zhang, L. Gu, B. V. Merinov, Z. Lin, E. Zhu, T. Yu, Q. Jia, J. Guo, L. Zhang, W. A. Goddard, Y. Huang and X. Duan, Ultrafine jagged platinum nanowires enable ultrahigh mass activity for the oxygen reduction reaction, *Science*, 2016, **354**, 1414–1419.

131 Y. Lu, S. Du and R. Steinberger-Wilckens, Three-dimensional catalyst electrodes based on PtPd nanodendrites for oxygen reduction reaction in PEFC applications, *Appl. Catal., B*, 2016, **187**, 108–114.

132 E. Fidiani, A. Z. Alkahfi, M. A. U. Absor, R. D. Pravitasari, Damisih, E. Listiani Dewi, Y. L. Chiu and S. Du, Au-Doped PtAg Nanorod Array Electrodes for Proton-Exchange Membrane Fuel Cells, *ACS Appl. Energy Mater.*, 2022, **5**, 14979–14989.

133 J. J. Conde, P. Ferreira-Aparicio and A. M. Chaparro, Electrospray Deposition: A Breakthrough Technique for Proton Exchange Membrane Fuel Cell Catalyst Layer Fabrication, *ACS Appl. Energy Mater.*, 2021, **4**, 7394–7404.

134 W. Wang, S. Chen, J. Li and W. Wang, Fabrication of catalyst coated membrane with screen printing method in a proton exchange membrane fuel cell, *Int. J. Hydrogen Energy*, 2015, **40**, 4649–4658.

135 P. Liu, D. Yang, B. Li, C. Zhang and P. Ming, Recent progress of catalyst ink for roll-to-roll manufacturing paired with slot die coating for proton exchange membrane fuel cells, *Int. J. Hydrogen Energy*, 2023, **48**, 19666–19685.

136 H. Liu, L. Ney, N. Zamel and X. Li, Effect of Catalyst Ink and Formation Process on the Multiscale Structure of Catalyst Layers in PEM Fuel Cells, *Appl. Sci.*, 2022, **12**, 1–41.

137 M. Wang, J. H. Park, S. Kabir, K. C. Neyerlin, N. N. Kariuki, H. Lv, V. R. Stamenkovic, D. J. Myers, M. Ulsh and S. A. Mauger, Impact of Catalyst Ink Dispersing Methodology on Fuel Cell Performance Using in-Situ X-ray Scattering, *ACS Appl. Energy Mater.*, 2019, **2**, 6417–6427.

138 Y. Guo, F. Pan, W. Chen, Z. Ding, D. Yang, B. Li, P. Ming and C. Zhang, *The Controllable Design of Catalyst Inks to Enhance PEMFC Performance: A Review*, Springer Singapore, 2021, vol. 4.

139 Z. Turtayeva, F. Xu, J. Dillet, K. Mozet, R. Peignier, A. Celzard and G. Maranzana, The Influence of Ink Formulation and Preparation on the Performance of Proton-Exchange Membrane Fuel Cell, *Energies*, 2023, **16**, 1–24.

140 M. Mohammadi, N. Mohammadi and S. Mehdipour-Ataei, On the preparation of thin nanofibers of polysulfone polyelectrolyte for improving conductivity of proton-

exchange membranes by electrospinning: Taguchi design, response surface methodology, and genetic algorithm, *Int. J. Hydrogen Energy*, 2020, **45**, 34110–34124.
141 M. Yusro and V. Hacker, Insight into aligned nanofibers improving fuel cell performances: strategies, rationalities, and opportunities, *Mater. Adv.*, 2024, 4974–4995.
142 M. Lu, J. Liang, W. Zhan, Y. Li, H. Chen, M. Li, S. Liao and Z. Cui, Corrosion Mechanism and Mitigation Strategies for Carbon Supports in PEMFCs, *Adv. Sustainable Syst.*, 2024, **2400742**, 1–29.
143 L. Duclos, R. Chattot, L. Dubau, P. X. Thivel, G. Mandil, V. Laforest, M. Bolloli, R. Vincent and L. Svecova, Closing the loop: Life cycle assessment and optimization of a PEMFC platinum-based catalyst recycling process, *Green Chem.*, 2020, **22**, 1919–1933.
144 R. Granados-Fernández, M. A. Montiel, S. Díaz-Abad, M. A. Rodrigo and J. Lobato, Platinum recovery techniques for a circular economy, *Catalysts*, 937, DOI: 10.3390/catal11080937.
145 R. Stropnik, A. Lotrič, A. Bernad Montenegro, M. Sekavčnik and M. Mori, Critical materials in PEMFC systems and a LCA analysis for the potential reduction of environmental impacts with EoL strategies, *Energy Sci. Eng.*, 2019, **7**, 2519–2539.
146 A. Valente, D. Iribarren and J. Dufour, End of life of fuel cells and hydrogen products: From technologies to strategies, *Int. J. Hydrogen Energy*, 2019, **44**, 20965–20977.
147 S. Y. Cha and W. M. Lee, Performance of Proton Exchange Membrane Fuel Cell Electrodes Prepared by Direct Deposition of Ultrathin Platinum on the Membrane Surface, *J. Electrochem. Soc.*, 1999, **146**, 4055–4060.
148 J. A. Singh, N. Yang and S. F. Bent, Nanoengineering heterogeneous catalysts by atomic layer deposition, *Annu. Rev. Chem. Biomol. Eng.*, 2017, **8**, 41–62.
149 S. Cavaliere, S. Subianto, I. Savych, D. J. Jones and J. Rozière, Electrospinning: Designed architectures for energy conversion and storage devices, *Energy Environ. Sci.*, 2011, **4**, 4761–4785.
150 Z. Dong, S. J. Kennedy and Y. Wu, Electrospinning materials for energy-related applications and devices, *J. Power Sources*, 2011, **196**, 4886–4904.
151 K. Waldrop, R. Wycisk and P. N. Pintauro, Application of electrospinning for the fabrication of proton-exchange membrane fuel cell electrodes, *Curr. Opin. Electrochem.*, 2020, **21**, 257–264.
152 S. Jiang, J. Li, J. Fang and X. Wang, Fibrous-Structured Freestanding Electrodes for Oxygen Electrocatalysis, *Small*, 2021, **17**, 1–24.
153 D. F. Van Der Vliet, C. Wang, D. Tripkovic, D. Strmcnik, X. F. Zhang, M. K. Debe, R. T. Atanasoski, N. M. Markovic and V. R. Stamenkovic, Mesostructured thin films as electrocatalysts with tunable composition and surface morphology, *Nat. Mater.*, 2012, **11**, 1051–1058.
154 M. K. Debe, Electrocatalyst approaches and challenges for automotive fuel cells, *Nature*, 2012, **486**, 43–51.
155 K. Wang and Y. Ding, Carbon-free nanoporous gold based membrane electrocatalysts for fuel cells, *Prog. Nat. Sci.:Mater. Int.*, 2020, **30**, 775–786.
156 Y. Ding, Y. J. Kim and J. Erlebacher, Nanoporous gold leaf: "Ancient technology"/advanced material, *Adv. Mater.*, 2004, **16**, 1897–1900.
157 Q. Sang, S. Hao, J. Han and Y. Ding, Dealloyed nanoporous materials for electrochemical energy conversion and storage, *EnergyChem*, 2022, **4**, 100069.
158 Y. Zeng, H. Zhang, Z. Wang, J. Jia, S. Miao, W. Song, Y. Xiao, H. Yu, Z. Shao and B. Yi, Nano-engineering of a 3D-ordered membrane electrode assembly with ultrathin Pt skin on open-walled PdCo nanotube arrays for fuel cells, *J. Mater. Chem. A*, 2018, **6**, 6521–6533.
159 M. K. Debe, A. Steinbach and K. Noda, Stop-Start and High-Current Durability Testing of Nanostructured Thin Film Catalysts for PEM Fuel Cells, *ECS Meeting Abstr.*, 2006, **MA2006-02**, 602.
160 M. K. Debe, A. K. Schmoeckel, G. D. Vernstrom and R. Atanasoski, High voltage stability of nanostructured thin film catalysts for PEM fuel cells, *J. Power Sources*, 2006, **161**, 1002–1011.
161 Q. Shao, K. Lu and X. Huang, Platinum Group Nanowires for Efficient Electrocatalysis, *Small Methods*, 2019, **3**, 1–22.
162 X. L. Tian, Y. Y. Xu, W. Zhang, T. Wu, B. Y. Xia and X. Wang, Unsupported Platinum-Based Electrocatalysts for Oxygen Reduction Reaction, *ACS Energy Lett.*, 2017, **2**, 2035–2043.
163 X. Li, L. Cong, H. Lin, F. Liu, X. Fu, H. C. Xu and N. Lin, Linear paired electrolysis of furfural to furoic acid at both anode and cathode in a multiple redox mediated system, *Green Energy Environ.*, 2024, **9**, 104–113.
164 P. Mardle, G. Thirunavukkarasu, S. Guan, Y. L. Chiu and S. Du, Comparative Study of PtNi Nanowire Array Electrodes toward Oxygen Reduction Reaction by Half-Cell Measurement and PEMFC Test, *ACS Appl. Mater. Interfaces*, 2020, **12**, 42832–42841.
165 S. Du, Recent Advances in Electrode Design Based on One-Dimensional Nanostructure Arrays for Proton Exchange Membrane Fuel Cell Applications, *Engineering*, 2021, **7**, 33–49.
166 K. Li, X. Li, H. Huang, L. Luo, X. Li, X. Yan, C. Ma, R. Si, J. Yang and J. Zeng, One-Nanometer-Thick PtNiRh Trimetallic Nanowires with Enhanced Oxygen Reduction Electrocatalysis in Acid Media: Integrating Multiple Advantages into One Catalyst, *J. Am. Chem. Soc.*, 2018, **140**, 16159–16167.
167 C. Li, H. Tan, J. Lin, X. Luo, S. Wang, J. You, Y. M. Kang, Y. Bando, Y. Yamauchi and J. Kim, Emerging Pt-based electrocatalysts with highly open nanoarchitectures for boosting oxygen reduction reaction, *Nano Today*, 2018, **21**, 91–105.
168 S. Y. Ma, H. H. Li, B. C. Hu, X. Cheng, Q. Q. Fu and S. H. Yu, Synthesis of Low Pt-Based Quaternary PtPdRuTe Nanotubes with Optimized Incorporation of Pd for Enhanced Electrocatalytic Activity, *J. Am. Chem. Soc.*, 2017, **139**, 5890–5895.

169 J. W. Jeong, S. R. Yang, Y. H. Hur, S. W. Kim, K. M. Baek, S. Yim, H. I. Jang, J. H. Park, S. Y. Lee, C. O. Park and Y. S. Jung, High-resolution nanotransfer printing applicable to diverse surfaces *via* interface-targeted adhesion switching, *Nat. Commun.*, 2014, **5**, 1–12.

170 S. Yim, S. Jeon, J. M. Kim, K. M. Baek, G. H. Lee, H. Kim, J. Shin and Y. S. Jung, Transferrable Plasmonic Au Thin Film Containing Sub-20 nm Nanohole Array Constructed *via* High-Resolution Polymer Self-Assembly and Nanotransfer Printing, *ACS Appl. Mater. Interfaces*, 2018, **10**, 2216–2223.

171 J. M. Kim, A. Jo, K. A. Lee, H. J. Han, Y. J. Kim, H. Y. Kim, G. R. Lee, M. Kim, Y. Park, Y. S. Kang, J. Jung, K. H. Chae, E. Lee, H. C. Ham, H. Ju, Y. S. Jung and J. Y. Kim, Conformation-modulated three-dimensional electrocatalysts for high-performance fuel cell electrodes, *Sci. Adv.*, 2021, **7**, 1–13.